

The H I content of extremely metal-deficient blue compact dwarf galaxies

T. X. Thuan¹, K. M. Goehring¹, J. E. Hibbard², Y. I. Izotov³ and L. K. Hunt⁴

¹*Astronomy Department, University of Virginia, P.O. Box 400325, Charlottesville, VA 22904-4325, USA; txt@virginia.edu, kmg4mx@virginia.edu*

²*National Radio Astronomy Observatory, Charlottesville, VA 22903, USA; jhibbard@nrao.edu*

³*Main Astronomical Observatory, National Academy of Sciences of Ukraine, 03680 Kyiv, Ukraine; izotov@mao.kiev.ua*

⁴*INAF-Osservatorio Astrofisico di Arcetri, Largo E. Fermi 5, I-50125 Firenze, Italy; hunt@arcetri.astro.it*

19 January 2015

ABSTRACT

We have obtained new H I observations with the 100 m Green Bank Telescope (GBT) for a sample of 29 extremely metal-deficient star-forming Blue Compact Dwarf (BCD) galaxies, selected from the Sloan Digital Sky Survey spectral data base to be extremely metal-deficient ($12 + \log \text{O/H} \leq 7.6$). Neutral hydrogen was detected in 28 galaxies, a 97% detection rate. Combining the H I data with SDSS optical spectra for the BCD sample and adding complementary galaxy samples from the literature to extend the metallicity and mass ranges, we have studied how the H I content of a galaxy varies with various global galaxian properties. There is a clear trend of increasing gas mass fraction with decreasing metallicity, mass and luminosity. We obtain the relation $M(\text{H I})/L_g \propto L_g^{-0.3}$, in agreement with previous studies based on samples with a smaller luminosity range. The median gas mass fraction f_{gas} for the GBT sample is equal to 0.94 while the mean gas mass fraction is 0.90 ± 0.15 , with a lower limit of ~ 0.65 . The H I depletion time is independent of metallicity, with a large scatter around the median value of 3.4 Gyr. The ratio of the baryonic mass to the dynamical mass of the metal-deficient BCDs varies from 0.05 to 0.80, with a median value of ~ 0.2 . About 65% of the BCDs in our sample have an effective yield larger than the true yield, implying that the neutral gas envelope in BCDs is more metal-deficient by a factor of 1.5–20, as compared to the ionized gas.

Key words: galaxies: dwarf – galaxies: fundamental parameters – galaxies: irregular – galaxies: ISM – galaxies: starburst

1 INTRODUCTION

The formation and evolution of the first galaxies in the universe remains a key issue in cosmology. It is now thought that large massive star-forming galaxies form in a hierarchical manner from the assembly of smaller dwarf systems, through accretion and merger processes. These galaxy interactions trigger the formation of stars which enrich the interstellar gas in metals by stellar winds and supernovae. In this scenario, the number of extremely metal-deficient (XMD) dwarf galaxies should be high in the early universe but considerably smaller at the present epoch (Mamon et al. 2012).

However, while much progress has been made in finding large populations of galaxies at high ($z \geq 3$) redshifts (e.g. Steidel et al. 2003; Adelberger et al. 2005), truly chemically unevolved galaxies remain elusive in the high- z universe. The spectra of distant galaxies generally indicate the presence of a substantial amount of heavy elements, implying

previous star formation and metal enrichment. The discovery of XMD galaxies at high z may have to wait until the advent of the *JWST* and 30 m-class ground-based telescopes.

We adopt here a different approach. Instead of searching for high- z metal-deficient objects, we focus our attention on XMD star-forming dwarf galaxies in the local universe. They are the most promising local proxies of chemically unevolved galaxies in the early universe, and are usually found among a class of dwarf galaxies undergoing intense bursts of star formation called Blue Compact Dwarf (BCD) galaxies (Thuan & Martin 1981). The optical spectra of the BCDs are characterized by a blue continuum on which are superimposed strong narrow emission lines. XMD BCDs are very rare (Izotov, Thuan & Guseva 2012). For more than three decades, one of the first BCD discovered, I Zw 18 (Sargent & Searle 1970), held the record as the most metal-deficient emission-line galaxy known, with an oxygen abundance $[\text{O/H}] = 12 + \log \text{O/H} = 7.17 \pm 0.01$ in

its northwestern component and 7.22 ± 0.02 in its southeastern component (Thuan & Izotov 2005) ($\sim 3\%$ solar, adopting the solar abundance $12 + \log O/H = 8.76$ of Steffen et al. 2015). Only in 2005 has I Zw 18 been superseded in its rank by SBS 0335–052W with a metallicity $[O/H] = 7.12$ (Izotov, Thuan & Guseva 2005).

Because of the scarcity of XMD emission-line galaxies, we stand a much better chance of discovering them in very large spectroscopic surveys such as the Sloan Digital Sky Survey (SDSS, York et al. 2000). We have carried out a systematic search for such objects with $[O/H]$ in the SDSS spectroscopic data release 7 (DR 7) (Abazajian et al. 2009). Imposing cut-offs in metallicity and redshift results in a total sample of 29 XMD BCDs. Similar searches for XMD galaxies in the SDSS have been carried out by Morales-Luis et al. (2011) and Sánchez Almeida et al. (2016). We found a total of 10 galaxies in common between the present sample and that of Sánchez Almeida et al. (2016) so that the two samples are likely to have similar properties, and the H I characteristics discussed here probably apply to the Sánchez Almeida et al. (2016) objects as well.

The focus of this paper is the study of the neutral hydrogen content of these XMD objects. There have been previous H I studies of this type of extremely metal-poor galaxies. Thus, Filho et al. (2013) have carried out a single-dish H I study with the Effelsberg radio telescope of a subsample of 29 XMD galaxies selected from the Morales-Luis et al. (2011) list. We will use part of the data of those authors to supplement our own and will compare with our results with theirs when warranted. A handful of interferometric H I maps of other XMD galaxies have also been obtained by the Pune group with the Giant Metrewave radio telescope (see Ekta, Pustilnik & Chengalur 2009; Ekta & Chengalur 2010, and references therein). In Section 2, we define the XMD BCD sample and describe observations of their neutral hydrogen content with the Robert C. Byrd Green Bank Telescope (GBT) at the National Radio Astronomy Observatory¹. This sample will be referred to hereafter as the GBT sample. Section 3 describes the H I data along with derived ancillary data such as metallicities, star formation rates, stellar masses needed to study trends of the neutral gas content with other properties of the BCDs. In Section 4, we discuss several comparison samples compiled from the literature, useful for studying the H I content of star-forming galaxies over a wider range of heavy element abundances and stellar masses. Our total galaxy sample, composed of the GBT and three comparison samples, includes 151 objects and covers the extensive metallicity range $7.20 \leq [O/H] \leq 8.76$. We study in Section 5 the correlations of various quantities. In particular, we analyze the dependence of the neutral gas mass to light ratio on metal abundance, and that of the gas mass fraction on stellar mass. We also discuss the chemical evolution of XMD BCDs. We summarize our conclusions in Section 6. Throughout this paper, we adopt the cosmological model characterized by a Hubble constant $H_0 = 73 \text{ km s}^{-1} \text{ Mpc}^{-1}$, a matter density parameter $\Omega_M = 0.27$

and a dark energy density parameter $\Omega_\Lambda = 0.73$ (Riess et al. 2011).

2 H I OBSERVATIONS

2.1 The GBT sample

We have constructed our XMD BCD sample by applying the following selection criteria to the SDSS DR7 spectral database. As described in Izotov et al. (2012), we first select them on the basis of the relative fluxes of particular emission lines as measured on the SDSS spectra: $[O \text{ III}]\lambda 4959/H\beta \leq 1$ and $[N \text{ II}]\lambda 6853/H\beta \leq 0.1$. These spectral properties select out uniquely low-metallicity dwarfs since no other type of galaxy possesses them. Second, since one of the main scientific objectives here is to study how the H I properties of star-forming galaxies vary with metallicity, it is important to have accurate heavy element abundances for the XMD BCDs. Thus, we have included in our sample only those BCDs that have a well-detected $[O \text{ III}]\lambda 4363$ line as this electron temperature-sensitive emission line allows a direct and precise abundance determination. Third, we have set a metallicity cut-off $[O/H] \leq 7.6$ ($\sim 8\%$ solar) to choose only XMD galaxies. This metallicity threshold has been suggested by Izotov & Thuan (1999) to characterize very young galaxies, with most of their stellar populations formed not more than ~ 1 Gyr ago. Lastly, we have chosen the BCDs to be not more distant than ~ 85 Mpc, so we can measure their H I emission with a good signal-to-noise ratio within a reasonable integration time with the GBT. This distance upper limit corresponds to a recession velocity of $\sim 6200 \text{ km s}^{-1}$. These selection criteria result in a total sample of 29 XMD BCDs. In contrast to many previous BCD samples that have been observed in H I (e.g. Thuan & Martin 1981; Thuan et al. 1999b; Huchtmeier, Krishna & Petrosian 2005; Filho et al. 2013), this BCD sample is unique in that : 1) it contains only very metal-deficient objects ($7.35 \leq [O/H] \leq 7.60$) as compared to previous samples which include many objects with $[O/H] \geq 7.7$. This allows us to study very chemically unevolved galaxies; 2) it has O abundances determined precisely for each object, using the direct method based on the $[O \text{ III}]\lambda 4363$ line. This is in contrast to the approximate abundances derived for many galaxies in previous samples, using the statistical strong-line method, because of the undetectability of the $[O \text{ III}]$ line; 3) all objects possess accurate SDSS images and photometry with which we can derive optical luminosities and mass-to-light ratios.

2.2 Observations and Data reduction

The observations were obtained with the 100 m GBT during the periods September 2005 and January–February 2006. The GBT spectrometer backend was used with a total bandwidth of 12.5 MHz and 9-level sampling, resulting in a total of 16,384 spectral channels. We use two spectral windows centered at the same frequency (1420.4058 MHz) with two different linear polarizations (XX and YY). Each target was observed in total power mode with multiple (between 2 and 6) 10 minute on-source, 10 minute off-source pairs. The total on-source time for each galaxy was determined during the observing runs, depending on the strength of the spectral

¹ The National Radio Astronomy Observatory is a facility of the National Science Foundation operated under cooperative agreement by Associated Universities, Inc.

feature relative to the noise. Since the two polarizations were detected independently, they were averaged to improve sensitivity. The data were flagged for radio frequency interference (RFI) and all scans summed. The data were calibrated by observations of standard continuum calibrators from the list of NRAO VLA Sky Survey unconfused calibrator sources prepared by J. Condon and Q.F. Yin, using the same back-end setup. We checked our calibration by observing standard spectral line calibrators from the list of [Hogg et al. \(2007\)](#) and found it to be good to $\sim 3\%$. All data reduction was done in GBTIDL. The data were boxcar-smoothed by 20 channels, for a final frequency resolution of 15.26 kHz, corresponding to a velocity resolution of ~ 3.3 km/s. RMS noise levels were 3 mJy for a single 10 minute on/off scan. Spectral baselines were fit using line-free channels and subtracted out. Generally, a low-order fit, between 1 and 3, was used. Line fluxes and linewidth at 20% and 50% of peak intensity were measured in IDL. Distances were calculated from the measured redshifts, after correcting for Virgo infall, using the Virgo-centric flow model of [Mould et al. \(2000\)](#).

Of the 29 XMD BCDs in our sample, 28 galaxies were detected. This corresponds to a 97% detection rate, considerably higher than those of previous BCD samples. For comparison, the detection rate of the [Thuan & Martin \(1981\)](#) sample is 80%, that of the [Thuan et al. \(1999b\)](#) sample 74%, and that of [Filho et al. \(2013\)](#) only 34%. The reason for the high detection rate of our GBT sample is probably the higher sensitivity of the present observations. Thus, the 5σ uncertainties of our observations are ~ 0.1 Jy km s $^{-1}$ while those of the [Filho et al. \(2013\)](#) observations are about 0.6 Jy km s $^{-1}$.

2.3 H I data

H I profiles (after boxcar smoothing and baseline removal) of all galaxies in the sample are presented in Fig. 1. There is only one non-detection, the BCD J2238+1400 = HS 2236+1344. The profiles are arranged from left to right and from top to bottom in order of increasing right ascension. In addition, Fig. 2 shows the SDSS image of each galaxy, taken from Data Release 10 (DR10, [Ahn et al. 2013](#)). The images are useful for examining the morphology and colors of the sample objects and for evaluating potential H I contamination from neighboring galaxies. It is clear that our objects are generally very compact, the average half-light g radius of the dwarf galaxies in our sample is about $10''$ (column 5 of Table 2), their linear diameters being generally less than 2 kpc. Adopting an average H I-to-optical size ratio of ~ 3 ([Thuan & Martin 1981](#)), the H I angular extent of all sample galaxies are considerably smaller than the $9'$ GBT beam at 21 cm, so we did not need to apply any beam correction to the flux densities. To check for potential contamination of the H I emission from neighboring galaxies, we have also examined the SDSS DR10 images in a square field of $12'$ on a side centered on each object. We have found no case of contamination. For J1214+0940 with $v = 1702$ km s $^{-1}$, there is a faint diffuse yellow galaxy at $4.5'$ of the BCD in the NW direction, but its velocity is 1245 km s $^{-1}$.

Observed and derived H I parameters for all detected galaxies (28 objects) are given in Table 1. Column 1 lists the galaxies in order of increasing right ascension (given in Table

2). Column 2 gives the integrated H I flux densities and their errors. The errors are taken to be equal to ([Thuan et al. 1999b](#))

$$\sigma = 2 \times \sqrt{N} \times RMS \times \Delta v, \quad (1)$$

where N is the number of channels over which the line is detected, RMS is the root-mean-square deviation in mJy in the baseline fit to the 20-channel boxcar smoothed 21 cm spectrum, as given in column 3, and Δv is the velocity resolution equal to 3.3 km s $^{-1}$.

We can use the measured RMS of 1.86 mJy of the spectrum of the non-detected galaxy J2238+1400, to derive an upper limit for its H I mass. This galaxy, at the distance of 86.4 Mpc, is the furthest object in our sample. We take its H I velocity width at zero intensity to be 192 km s $^{-1}$, obtained by multiplying 155 km s $^{-1}$, the largest Δv_{20} in our sample (Table 1), by 1.2, assuming that the velocity width at zero intensity is 20% wider than Δv_{20} . Assuming a rectangular profile, we obtain a 5σ upper limit $M(\text{H I}) \leq 3.1 \times 10^9 M_{\odot}$.

Columns 4 and 5 give respectively the velocity widths at 20% of maximum intensity and the mid-point velocities of the 20% profile widths, while columns 6 and 7 list the same quantities at 50% of maximum intensity. Column 8 lists H I masses calculated from the integrated line flux densities using the equation

$$M(\text{H I}) = 2.36 \times 10^5 \int S dv D^2 M_{\odot}, \quad (2)$$

where D is the distance in Mpc given in column 3 of Table 2 and $\int S dv$ is the integrated H I flux density in Jy km s $^{-1}$, given in column 2.

Column 9 gives the logarithm of the ratio of the H I mass to absolute g luminosity of each galaxy. The luminosity is given in column 4 of Table 2, and we adopt $M_{g,\odot} = 5.12$ mag ([Bessel 2005](#)).

2.4 Shapes of H I profiles and galaxy morphologies

Column 10 gives the classification of each H I profile. We have classified the H I profiles into two broad categories, depending on their shapes: the Gaussian (G) profiles characteristic of diskless dwarf galaxies without large rotational motions, and the steep-sided double-horn (DH) profiles characteristic of inclined disk galaxies with significant rotational motions. The reliability of the profile classification depends on the signal-to-noise ratio of the spectrum, decreasing with lower values of that ratio. Most of the H I profiles (20 out of 28, or 71%) have a Gaussian shape, indicating dominant random motions, while the remaining have double-horned profiles, reflecting dominant rotational motions.

We have examined the morphology of all galaxies in the sample using the SDSS images (Fig. 2). Using the classification terminology of [Sánchez Almeida et al. \(2016\)](#), we find 3 galaxies (J0133+1343, J1055+5111 and J1201+0211) or 10% of the sample to be symmetric, with a centrally concentrated emission, 3 galaxies (J1044+0353, J1202+5415 and J2238+1400) possessing 2 knots (10%), 5 galaxies (J0908+0517, J0944+0936, J1148+5400, J1150+5627 and J1335+4910) having multiple knots (17%) and the remaining 18 galaxies (63%) having a cometary structure. According to the BCD morphological classification scheme of

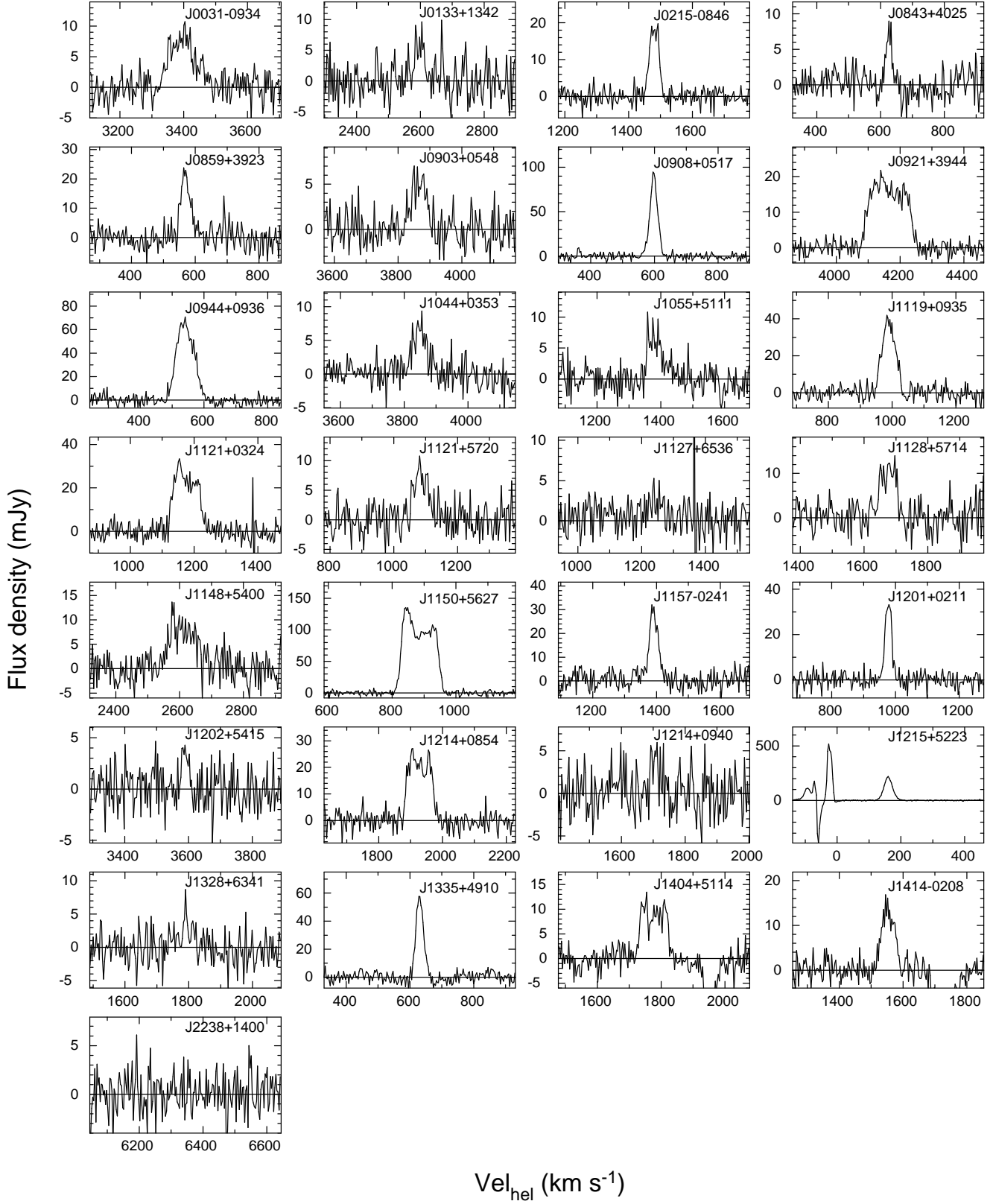


Figure 1. H I profiles of the 29 galaxies observed with the GBT. Profiles are arranged, from top left to bottom right, in order of increasing right ascension.

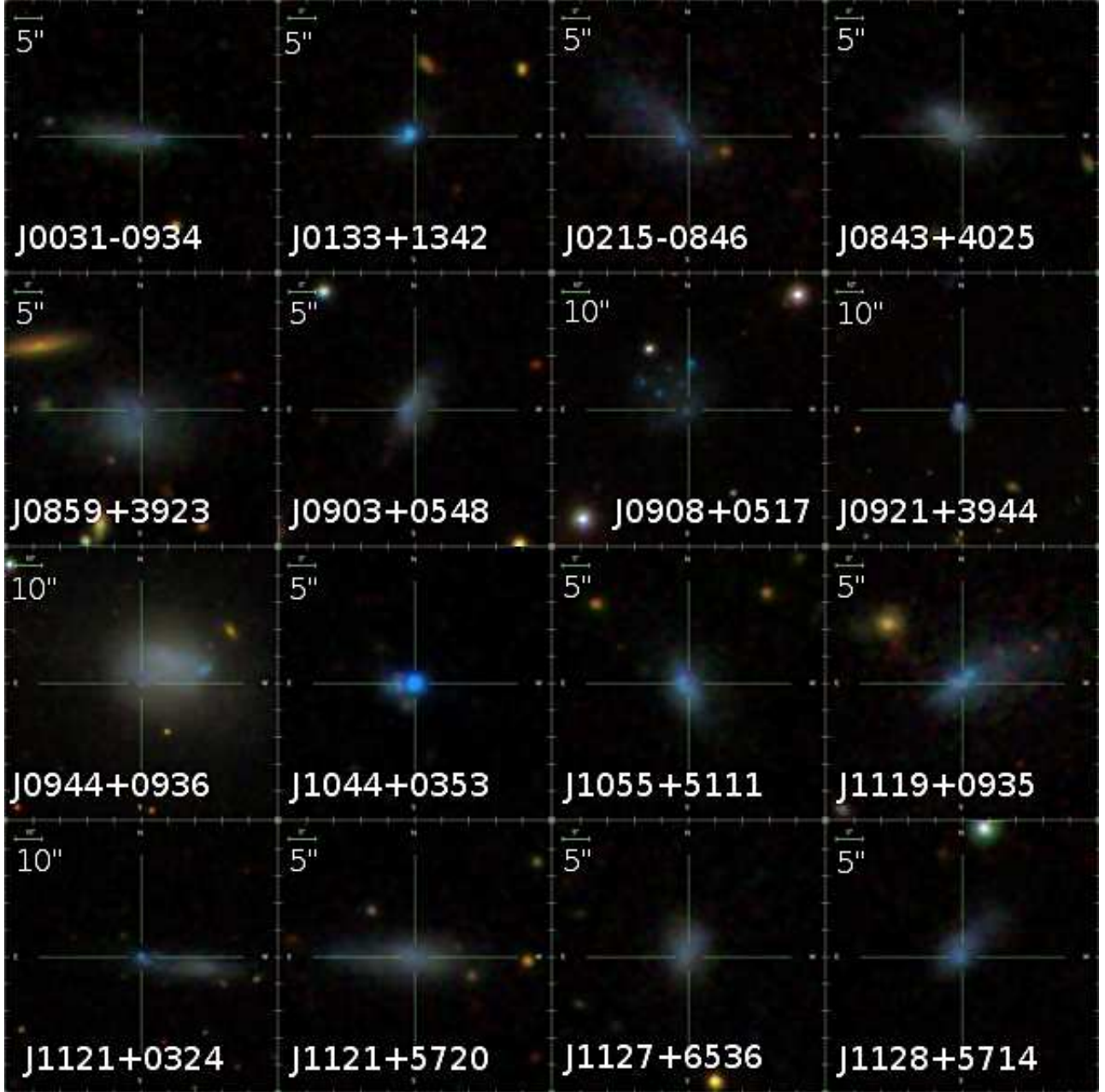


Figure 2. SDSS images of the BCDs whose H I profiles are shown in Fig.1. North is on top and East to the left. The scale is shown by a horizontal bar.

Loose & Thuan (1985), the cometary BCDs are characterized by a high surface brightness star-forming region (the comet’s “head”) located near one end of an elongated lower surface brightness stellar body (the comet’s “tail”). The latter could be interpreted as a rotating thin stellar disk seen nearly edge-on, but with modest rotational velocities and significant random motions, as suggested by the predominance of the H I profiles with a Gaussian shape. It is interesting that the low-metallicity selection criterion has picked out a majority of cometary BCDs. How does the optical morphology classification of the GBT sample compare with that of other XMD samples such as the one assembled by Morales-Luis et al. (2011)? These authors also find in their XMD sample a predominance of cometary mor-

phology (75%), the remaining 25% showing a single knot without any obvious underlying low-surface brightness component. Sánchez Almeida et al. (2016) found in their XMD sample that 57% of the galaxies are cometary, with 23% symmetric, 10% multi-knot and 4% 2-knot. The common feature of all these XMD samples is that they all show a large proportion (more than half) of cometary galaxies. Recently, Sánchez Almeida et al. (2015) have suggested that these metal-deficient cometary galaxies are the result of low-metallicity gas clouds falling onto low-surface-brightness galaxy disks, and triggering bursts of star formation. The star-forming regions tend to be at the ends of the low-surface-brightness disks because the impacting gas clouds

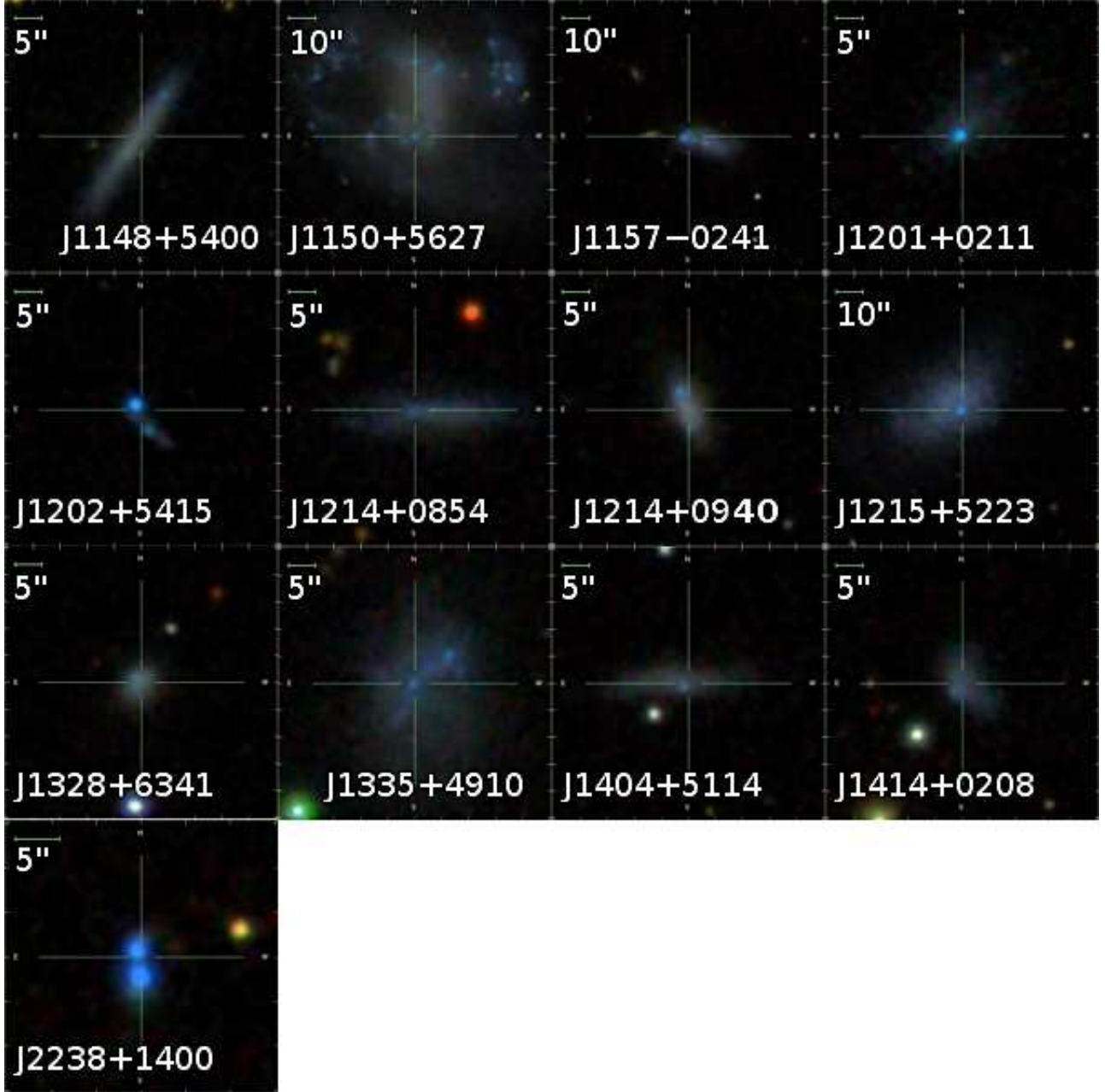


Figure 2. (Continued)

have the largest effects on the outer parts of galaxies where the ambient pressure and column density are low.

2.5 Comparison with previous H I observations

A few galaxies in our sample have had previous H I observations. They are J0133+1342, J1121+0324, J1201+0211, J1215+5233 and J1202+5415 (Filho et al. 2013), J0944+0936 (Stierwalt et al. 2009), J0908+0517 and J1119+0935 (Popping & Braun 2011), J1121+0324, J1201+0211 and J1215+5223 (Pustilnik & Martin 2007), and J1214+0940 (Kent et al. 2008). Within the errors, our flux densities are in good general agreement with those of previous authors, except for two objects: J1215+5223 for

which Filho et al. (2013) found 4.7 ± 0.5 Jy km s⁻¹ and Pustilnik & Martin (2007) found 5.2 ± 0.2 Jy km s⁻¹ as compared to our flux density of 7.1 Jy km s⁻¹, and J1119+0935 for which Popping & Braun (2011) found a flux density of 1.4 ± 0.1 Jy km s⁻¹ as compared to our value of 1.9 ± 0.1 Jy km s⁻¹. These measurements were made with telescopes having similar beam sizes so the cause of the discrepancies is not clear.

3 SUPPLEMENTAL DATA

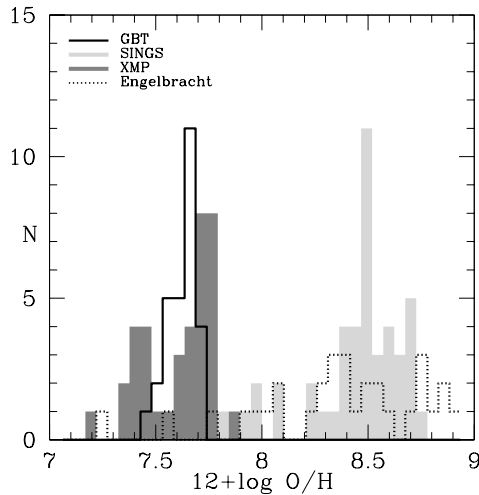
We have also listed in Table 2 other data, useful for characterizing the evolutionary state and star-forming properties

Table 1. GBT Objects, HI Data

Object	Sdv (Jy km s ⁻¹)	RMS (mJy)	Δv_{20} (km s ⁻¹)	v_{20} (km s ⁻¹)	Δv_{50} (km s ⁻¹)	v_{50} (km s ⁻¹)	$\log M(\text{H I})$ (M _⊙)	$\log M(\text{H I})/L_g$ (M _⊙ / L _⊙)	Profile Shape
(1)	(2)	(3)	(4)	(5)	(6)	(7)	(8)	(9)	(10)
J0031-0934	0.790 ± 0.097	2.05	134	3398	75	3386	8.60	0.400	DH
J0133+1342	0.208 ± 0.078	2.95	43	2596	31	2598	7.80	-0.191	G
J0215-0846	0.666 ± 0.056	1.85	51	1480	35	1481	7.78	0.204	G
J0843+4025	0.220 ± 0.060	2.14	23	629	16	628	6.80	-0.256	G
J0859+3923	0.806 ± 0.088	2.68	52	572	39	567	7.30	0.057	G
J0903+0548	0.297 ± 0.060	1.79	75	3862	51	3868	8.30	0.013	G
J0908+0517	2.712 ± 0.109	3.38	43	599	27	598	7.42	1.01	G
J0921+3944	2.351 ± 0.098	1.85	155	4165	136	4166	9.30	0.769	DH
J0944+0936	4.414 ± 0.128	3.07	91	542	70	543	7.48	-0.316	G
J1044+0353	0.373 ± 0.058	1.61	51	3849	41	3845	8.40	-0.099	G
J1055+5111	0.418 ± 0.060	1.55	82	1394	46	1378	7.74	-0.184	G
J1119+0935	1.959 ± 0.116	3.33	73	990	51	991	7.83	0.187	G
J1121+0324	2.378 ± 0.118	2.75	106	1175	89	1176	8.35	0.770	DH
J1121+5720	0.424 ± 0.082	2.48	67	1086	56	1081	7.66	-0.107	G
J1127+6536	0.157 ± 0.071	2.00	53	1246	52	1247	7.25	-0.365	G
J1128+5714	0.648 ± 0.134	3.82	66	1675	61	1676	8.08	0.316	DH
J1148+5400	0.869 ± 0.091	2.01	108	2614	92	2619	8.51	0.389	DH
J1150+5627	12.99 ± 0.122	2.89	134	888	118	886	8.95	0.731	DH
J1157-0241	1.065 ± 0.114	3.25	44	1392	32	1392	8.15	0.548	G
J1201+0211	0.869 ± 0.104	3.42	32	976	26	977	7.18	0.206	G
J1202+5415	0.093 ± 0.043	1.80	32	3589	29	3590	7.79	-0.231	G
J1214+0854	1.919 ± 0.120	2.98	97	1928	87	1929	7.89	0.750	DH
J1214+0940	0.118 ± 0.051	2.23	28	1702	26	1702	6.68	-0.688	G
J1215+5223	7.077 ± 0.089	2.56	47	161	30	160	7.27	0.187	G
J1328+6341	0.193 ± 0.073	1.86	59	1789	13	1790	7.61	-0.152	G
J1335+4910	1.680 ± 0.094	3.03	44	632	27	631	7.83	0.211	G
J1404+5114	1.008 ± 0.069	1.68	103	1774	92	1778	8.30	0.415	DH
J1414-0208	0.670 ± 0.075	2.29	65	1556	48	1554	7.99	0.347	G
J2238+1400	...	1.86	≤9.5

Notes: The columns are as follows. (1): Source name. Some of the objects are known under other names: J0944+0936 = IC559;

J1202+5415 = SBS1159+545; J1215+5223 = CGCG269-049; (2): H I integrated flux density and error. (3): Root-mean-square deviation in the baseline fit. (4): H I line width at 20% of the peak flux density. (5): Velocity at 20% of maximum. (6): H I line width at 50% of the peak flux density. (7): Velocity at 50% of maximum. (8): H I gas mass. (9): Ratio of H I gas mass to g -band luminosity. (10): G= Gaussian profile; DH= Double-horned profile.


Figure 3. Histogram of oxygen abundance for the GBT and the 3 comparison XMP, SINGS and Engelbracht samples.

of the 28 detected galaxies. Column 2 gives the J2000 coordinates of each galaxy. Column 3 gives the redshift as ob-

tained from the emission lines in the optical spectra (lower line) and the distance derived from the redshift corrected for Virgo infall (upper line) Column 4 gives the apparent (upper line) and absolute (lower line) g -band magnitudes within the galaxy's Petrosian 90% radius, as taken from the SDSS DR10. Column 5 lists the Petrosian 90% angular (upper line) and linear (lower line) radii, as taken from the SDSS DR10. To check the reliability of the photometric measurements of magnitudes and radii of the SDSS DR10, we have inspected visually all objects in the GBT sample and derived independently their g angular radii r_g . For 21 out of 28 objects (75%), our measured radii agree to within 10% with the SDSS DR10 radii. However, there are large discrepancies for 7 objects, the SDSS radius being too small as compared to our measured radius. These objects are J0908+0157, J0944+0936 = IC 559, J1044+0353, J1121+0324, J1148+5400, J1202+5415 and J1335+4910. With the exception of J1121+0324 that has a cometary structure, all of these objects have either a 2- or multi-knot structure. Evidently, the SDSS surface photometry routine does not handle well a multi-knot structure and derives radii and magnitudes for a single H II region rather than for the whole object. For these 7 objects, to make sure that our

Table 2. GBT Objects, Optical Data.

Object	RA Dec (J2000)	$D(\text{Mpc})$ z	m_g M_g	$r_g('')$ $R_g(\text{kpc})$	$[\text{O}/\text{H}]$ $i(^{\circ})$	$\log \text{SFR}$ ($\text{M}_{\odot} \text{ yr}^{-1}$) $\log f_{\text{cor}}$	$\log M_{*}$ $\log M_y$ (M_{\odot})	$\log M_{\text{dyn}}(\text{M}_{\odot})$ $M(\text{H I})/M_{\text{dyn}}$	$\log \tau(\text{yr})$ f_{gas}
(1)	(2)	(3)	(4)	(5)	(6)	(7)	(8)	(9)	(10)
J0031–0934	00:31:40	46.2	17.94	8.07	7.55	-1.05	7.719	9.75	9.565
	–09:34:34	0.0113	-15.38	1.81	70.1	0.952	5.952	0.071	0.914
J0133+1342	01:33:52	36.1	17.92	5.30	7.55	-1.07	6.639	8.52	8.87
	+13:42:09	0.0087	-14.87	0.93	81.9	0.488	5.743	0.190	0.954
J0215–0846	02:15:13	19.5	17.64	12.10	7.58	-1.93	6.826	8.72	9.71
	–08:46:24	0.0050	-13.81	1.14	42.8	0.900	5.188	0.116	0.936
J0843+4025	08:43:37	10.17	17.51	8.45	7.44	-2.80	6.395	7.60	9.60
	+40:25:46	0.0020	-12.53	0.42	58.2	0.928	4.748	0.158	0.782
J0859+3923	08:59:46	10.2	17.06	10.29	7.38	-2.74	7.154	8.46	10.04
	+39:23:06	0.0020	-12.98	0.51	42.8	1.252	4.766	0.069	0.660
J0903+0548	09:03:00	53.1	18.04	8.03	7.55	-1.08	7.684	9.30	9.38
	+05:48:23	0.0129	-15.59	2.07	65.5	0.772	5.896	0.100	0.852
J0908+0517	09:08:36	6.45	16.46	15.0	7.39	-3.158	5.658	8.10	10.58
	+05:17:27	0.0020	-12.59	0.47	56.1	0.672	3.886	0.209	0.988
J0921+3944	09:21:19	59.7	17.68	7.65	7.50	-1.03	7.494	10.33	10.33
	+39:44:59	0.0140	-16.20	2.21	73.7	0.736	5.877	0.093	0.989
J0944+0936	09:44:44	5.39	14.29	22.0	7.49	9.02	...
	+09:36:49	0.0018	-14.37	0.58	65.5	0.029	...
J1044+0353	10:44:57	53.7	17.16	5.5	7.46	-0.360	6.398	8.95	8.76
	+03:53:13	0.0129	-16.49	1.43	34.8	0.140	6.385	0.282	0.993
J1055+5111	10:55:08	23.5	17.53	8.76	7.59	-1.73	6.708	8.90	9.47
	+51:11:19	0.0046	-14.33	1.00	61.6	0.788	6.343	0.069	0.937
J1119+0935	11:19:28	12.1	16.42	15.52	7.52	-1.95	6.323	8.95	9.78
	+09:35:44	0.0033	-13.99	0.91	66.9	0.924	4.977	0.076	0.978
J1121+0324	11:21:52	20.0	16.56	24.5	7.56	-2.162	6.169	10.09	10.51
	+03:24:21	0.0041	-14.95	2.38	59.3	0.448	5.072	0.018	0.995
J1121+5720	11:21:47	21.3	17.35	11.18	7.55	-2.32	6.909	9.13	9.98
	+57:20:48	0.0036	-14.29	1.15	75.9	1.024	4.950	0.034	0.887
J1127+6536	11:27:17	21.9	17.79	7.82	7.46	-1.74	6.862	8.92	8.99
	+65:36:03	0.0041	-13.91	0.83	48.6	0.912	5.341	0.021	0.773
J1128+5714	11:28:24	27.9	17.95	9.19	7.55	-1.71	6.640	9.45	9.79
	+57:14:48	0.0056	-14.28	1.24	62.9	0.800	5.824	0.043	0.974

Table 2. Continued

Object	RA Dec (J2000)	$D(\text{Mpc})$ z	m_g M_g	$r_g(\prime\prime)$ $R_g(\text{kpc})$	[O/H] $i(^{\circ})$	$\log \text{SFR}$ ($M_{\odot} \text{ yr}^{-1}$) $\log f_{\text{cor}}$	$\log M_{\star}$ $\log M_y$ (M_{\odot})	$\log M_{\text{dyn}}(M_{\odot})$ $M(\text{H I})/M_{\text{dyn}}$	$\log \tau(\text{yr})$ f_{gas}
(1)	(2)	(3)	(4)	(5)	(6)	(7)	(8)	(9)	(10)
J1148+5400	11:48:01	39.7	17.13	13.7	7.54	10.11	...
	+54:00:19	0.0086	-15.86	2.64	65.5	0.025	...
J1150+5627	11:50:47	17.0	15.73	21.78	7.47	-1.59	7.415	10.80	10.54
	+56:27:06	0.0030	-15.42	1.80	26.1	1.660	5.681	0.014	0.909
J1157-0241	11:57:12	23.8	17.99	13.29	7.57	-1.69	6.379	8.77	9.84
	-02:41:11	0.0047	-13.89	1.53	56.1	0.636	5.868	0.240	0.988
J1201+0211	12:01:22	8.6	17.70	11.71	7.51	-1.20	6.131	8.09	8.38
	+02:11:08	0.0033	-11.97	0.49	51.3	0.688	5.643	0.123	0.940
J1202+5415	12:02:02	53.3	18.21	5.8	7.50	-0.788	6.295	8.67	8.58
	+54:15:50	0.0120	-15.42	1.50	28.7	0.192	5.892	0.132	0.978
J1214+0854	12:14:13	13.1	17.86	10.84	7.57	-1.25	7.053	9.41	9.14
	+08:54:30	0.0064	-12.73	0.69	81.9	1.204	5.821	0.030	0.906
J1214+0940	12:14:53	13.1	17.29	5.87	7.55	-2.05	7.258	7.97	8.73
	+09:40:11	0.0056	-13.30	0.37	61.6	0.848	5.813	0.051	0.270
J1215+5223	12:15:46	3.33	15.03	30.62	7.47	-3.49	6.027	8.22	10.76
	+52:23:14	0.005	-12.58	0.49	12.1	1.532	5.055	0.112	0.961
J1328+6341	13:28:22	29.8	18.09	6.87	7.56	-1.71	7.033	7.80	9.32
	+63:41:07	0.0060	-14.28	0.99	39.8	0.724	6.378	0.631	0.840
J1335+4910	13:35:42	13.01	16.23	10.38	7.60	-3.09	5.177	8.25	10.92
	+49:10:35	0.0022	-14.34	0.65	30.7	0.168	3.838	0.380	0.998
J1404+5114	14:04:32	29.1	17.72	11.87	7.58	-1.70	7.096	9.84	10.00
	+51:14:05	0.0058	-14.60	1.67	81.9	1.004	5.263	0.029	0.958
J1414-0208	14:14:54	24.9	17.99	7.33	7.35	-1.86	7.056	8.88	9.85
	-02:08:22	0.0051	-13.99	0.88	41.3	0.932	5.447	0.129	0.923

Notes: The columns are as follows. (1): Source name. (2): Right ascension and declination. (3): Distance in megaparsecs and optical redshift. (4): Apparent and absolute SDSS g -band Petrosian magnitude. (5): Optical major-axis radius, in arcseconds and kiloparsecs, containing 90% of the g -band light. From the SDSS. (6) Oxygen abundance $12+\log \text{O/H}$ and inclination angle of the source derived from the SDSS axial ratio. (7): Logarithm of the star formation rate. (8): Logarithm of the young and total stellar masses. (9): Logarithm of the dynamical mass derived from the g -band Petrosian radius. (10): Logarithm of the depletion time scale and the gas mass fraction.

derived r_g refers not only to the size of an individual H II region, but to that of the whole galaxy, we have derived by surface photometry our own g angular radii containing 90% of the total light and the magnitudes within these radii using the IRAF/APPHOT routine².

² IRAF is distributed by the National Optical Astronomy Observatories, which are operated by the Association of Universities for Research in Astronomy, Inc., under cooperative agreement with the National Science Foundation

Column 6 (upper line) gives for each galaxy the oxygen abundance [O/H]. As our galaxies were selected to possess a well-detected [O III] $\lambda 4363$ emission line in their spectra, these abundances are well determined, using the direct method. The derived oxygen abundances are generally those of the brightest H II region in the galaxy, typically the SDSS spectroscopic target. This however is a good indicator of the metallicity of the whole BCD as detailed spatial metallicity studies of a few of these objects show no evidence of large

metallicity gradients (e. g. [Thuan, Izotov & Foltz 1999a](#); [Noeske et al. 2000](#)).

Column 6 (lower line) gives the the inclination angle i in degrees of the plane of the galaxy to the plane of the sky ($i = 0$ for face-on and $i = 90^\circ$ for edge-on). Following [Thuan & Martin \(1981\)](#), i is calculated from

$$\cos^2 i = \frac{r_{25}^2 - r_0^2}{1 - r_0^2}, \quad (3)$$

where r_{25} is the axial ratio as obtained from the SDSS DR10 and r_0 is the intrinsic axial ratio of the galaxy. Following [Filho et al. \(2013\)](#), we adopt $r_0=0.25$, i.e. if a galaxy's disk appears more than four times elongated than wide, then its inclination angle is set to 90° . This relatively large value is motivated by the work of [Sánchez-Janssen, Méndez-Abreu & Aguerri \(2010\)](#) who identified a limiting stellar mass $M_* \sim 2 \times 10^9 M_\odot$ below which low-mass galaxies become systematically thicker because of the increasing importance of turbulent motions relative to rotational motions. The stellar masses of the GBT galaxies are all lower than this limiting mass, so this value is appropriate.

Column 7 gives the galaxy's present star formation rate (SFR) as derived from the extinction-corrected H α fluxes using [Kennicutt \(1998\)](#)'s relation:

$$\text{SFR}(M_\odot \text{ yr}^{-1}) = \frac{L(\text{H}\alpha)}{1.26 \times 10^{41} \text{ erg s}^{-1}}. \quad (4)$$

As the H α fluxes have been derived from SDSS spectra obtained with fibers of $3''$ diameter, we need to correct these SFRs for aperture effects. We have multiplied each SFR by a correction factor f equal to the ratio of the total flux to the flux within a $3''$ aperture:

$$f_{\text{cor}} = 10^{-0.4 \times [m_r(\text{tot}) - m_r(3'')]}, \quad (5)$$

where $m_r(\text{tot})$ and $m_r(3'')$ are respectively the r magnitudes within the Petrosian 90% radius and $3''$ fiber diameter, as given in the SDSS (we have used r magnitudes because the Finding Chart site of the SDSS DR10 gives magnitudes within the $3''$ fiber diameter only for the r band). The logarithm of f_{cor} is given in the lower line of column 7. Except for four galaxies, all have $\log f_{\text{cor}} \leq 1.0$. The two galaxies J0944+0936 and J1148+5400 have a large difference between $m_r(\text{tot})$ and $m_r(3'')$ (more than 4.5 mag), and hence large uncertain aperture corrections. We have thus decided not to include their SFRs in our statistical studies.

Column 8 gives the total stellar mass M_* and the young (age < 10 Myr) stellar mass M_y in units of solar masses, derived by model-fitting the spectral energy distribution (SED) of each galaxy, as described in [Izotov, Guseva & Thuan \(2011\)](#) and more recently in [Izotov et al. \(2016\)](#). As all our objects show strong line emission, care was taken in deriving these stellar masses to subtract the ionized gas emission. Neglecting this correction would result in a significant overestimate of the galaxy stellar mass. As the M_* are derived from spectra obtained with $3''$ diameter fibers, we have also applied to each M_* and M_y the upwards correction factor defined by Eq. 5. Like the SFRs, the M_* of the galaxies J0944+0936 and J1148+5400 are not included in our statistical studies because of their large uncertain aperture corrections.

To check the reliability of our derived SFRs and

M_* concerning the statistical studies in this paper, we have compared them with those obtained by the Max Planck Institute for Astrophysics – Johns Hopkins University (MPA-JHU) group ([Kauffmann et al. \(2003\)](#) and [Brinchmann et al. \(2004\)](#)). This constitutes a good check as the MPA-JHU group derives SFRs and M_* from total photometric magnitudes and thus does not have to apply aperture corrections as done here. We have found a very good statistical relation between the MPA-JHU SFRs and M_* and our aperture-corrected quantities. In a plot of M_* (MPA-JHU) vs. M_* (our group), the points scatter nicely along the equality line, with a dispersion of ~ 0.6 in $\log M_*$. The same holds for SFRs, with a dispersion of 0.2 in $\log \text{SFR}$. We thus conclude that our aperture-corrected quantities are quite adequate for the statistical studies described here and do not introduce any systematic bias.

Column 9 (upper line) gives an estimate of the dynamical mass M_{dyn} of each galaxy. We emphasize that these dynamical masses are only approximate. However they may help to reveal potentially interesting trends. M_{dyn} is calculated in the following way. For galaxies with rotation, characterized by a double-horned H I profile, the dynamical mass is estimated according to the following equation, derived by assuming an object in dynamical virial equilibrium where the gravitational force is balanced by the centrifugal force due to rotation:

$$M_{\text{dyn}}(M_\odot) = F \times 2.3 \times 10^5 v_c^2 (\text{km s}^{-1}) R(\text{HI}) (\text{kpc}). \quad (6)$$

Here F is a multiplicative factor that takes into account the degree of flattening of the galaxy. [Lequeux \(1983\)](#) has shown that F varies between 0.6 for a flat disk system and 1 for a spherical system. We adopt here $F = 0.7$ which corresponds to a flat disk with a flat rotation curve. $R(\text{H I})$ is the radius of the H I gas component. It is generally larger than the optical radius of the stellar component in the case of dwarf galaxies. From interferometric H I maps of several BCDs, [Thuan & Martin \(1981\)](#) have derived the approximate relation

$$R(\text{HI}) = 3 \times R_g, \quad (7)$$

which we adopt. Here, R_g is the Petrosian g -band 90% linear radius (column 5). v_c is the galaxy's rotational velocity corrected for inclination i (column 6):

$$v_c = \frac{v}{\sin i} = \frac{\Delta v_{50}/2}{\sin i}, \quad (8)$$

where v is the galaxy's observed rotational velocity, set to be equal to half of the velocity width at 50% of maximum intensity (column 6 of Table 1).

For galaxies with weak rotation, in virial equilibrium, supported against gravitational collapse by random motions, and characterized by a Gaussian H I profile, we estimate the dynamical mass by:

$$M_{\text{dyn}}(M_\odot) = 2.3 \times 10^5 \sigma^2 (\text{km s}^{-1}) R(\text{HI}) (\text{kpc}). \quad (9)$$

Here σ is the gas velocity dispersion where

$$\sigma = \sqrt{3} \times \Delta v_{50}/2.36. \quad (10)$$

The factor $\sqrt{3}$ converts the 1-dimensional velocity dispersion based on the H I velocity width to a 3-dimensional velocity dispersion, and the factor $1/2.36$ converts the Full Width at Half Maximum (FWHM) Δv of the Gaussian profile to a

velocity dispersion. Column 9 (lower line) gives the ratio of the H I mass to the dynamical mass.

Finally, column 10 (upper line) gives the gas depletion timescale $\tau = M(\text{H I})/\text{SFR}$ in units of log (yr). Column 10 (lower line) gives the gas mass fraction defined as

$$f_{\text{gas}} = \frac{M_{\text{gas}}}{M_{\text{baryon}}}, \quad (11)$$

where

$$M_{\text{gas}} = 1.4 \times M(\text{H I}). \quad (12)$$

The multiplicative factor 1.4 takes into account the masses of helium and metals. We do not include a correction for molecular hydrogen (H_2) as we have no H_2 observational constraints in these galaxies, and they are almost certainly H I-dominated.

M_{baryon} is the baryonic mass, defined as the sum of the gaseous and stellar masses:

$$M_{\text{baryon}} = M_{\text{gas}} + M_*. \quad (13)$$

4 COMPARISON SAMPLES

One of the main aims of this paper is to study how the H I content of a galaxy varies statistically with various global galaxian properties such as metallicity, SFR or stellar mass. To this end, the 28 galaxies in our GBT sample are not sufficient. As mentioned before, this sample spans only a very narrow range of oxygen abundances: $7.35 \leq [\text{O}/\text{H}] \leq 7.60$. We need to supplement our data on the GBT sample with data on other galaxy samples that span a larger metallicity range. Because of the mass-metallicity relation of galaxies, this means that the galaxian mass range will also be extended. We have thus searched the literature for other galaxy samples that possess data of the same nature as the GBT sample, but which span a larger range in metallicity and stellar mass, so that statistical trends can be studied. We have chosen three additional samples for comparison with the GBT sample.

The first sample consists of a subsample of the extremely metal-poor (XMP) galaxy sample of [Filho et al. \(2013\)](#) and [Morales-Luis et al. \(2011\)](#). Out of the 140 objects studied by these authors, there are 39 galaxies with the necessary ancillary data (oxygen abundances, derived using either the direct or strong-line methods, and H I fluxes), forming what will be called hereafter the ‘XMP sample’. This sample extends the metallicity range at the low-end (to $[\text{O}/\text{H}] = 7.07$) and augments the number of very low-metallicity galaxies, leading to better statistics in the low-metallicity range. The relevant data for the XMP sample is given in Table 3.

The second galaxy sample is that of [Engelbracht et al. \(2008\)](#). This sample was assembled to study metallicity effects on dust properties in starbursting galaxies so it is useful for our purposes as it spans a large metallicity range. We have added 31 objects from their study (those with oxygen abundances and H I measurements, and which are not already present in the XMP sample). They form what will be called hereafter the Engelbracht sample. The relevant data for that sample are given in Table 4. It spans the metallicity range $7.20 \leq [\text{O}/\text{H}] \leq 8.76$.

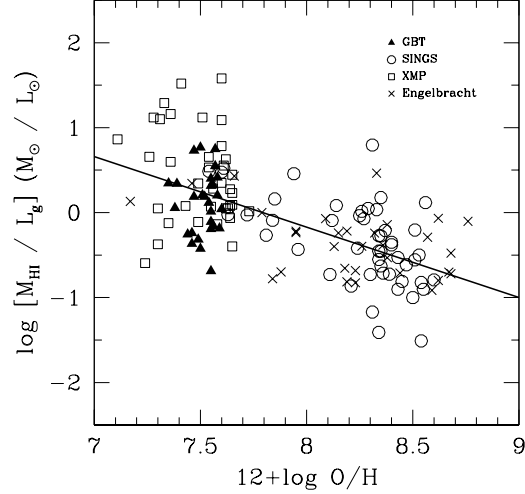


Figure 4. Plot of $M(\text{H I})/L_g$ versus oxygen abundance for the GBT and the 3 comparison samples. The solid line shows the least-square fit.

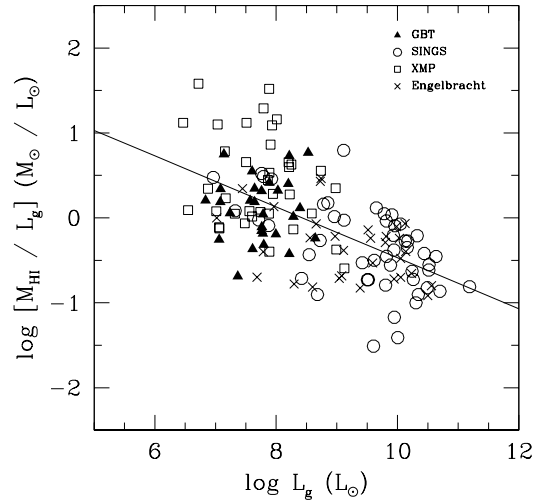


Figure 5. Plot of $M(\text{H I})/L_g$ versus absolute g magnitude for the GBT and the 3 comparison samples. The solid line shows the least-square fit.

Finally, we have added a third galaxy sample, assembled from the *SIRTF* Nearby Galaxy Sample (SINGS) of [Kennicutt et al. \(2003\)](#), hereafter called the SINGS sample. This sample is useful for increasing the number of galaxies and hence the statistics in the high mass and metallicity ranges. Selecting the galaxies with available oxygen abundances and H I fluxes results in a sample of 53 galaxies. The relevant data for the SINGS galaxies is given in Table 5.

The majority of the galaxies in the Engelbracht and SINGS samples do not possess m_g but m_B . To convert m_B into m_g , we have used the following transformation equation from [Jester et al. \(2005\)](#):

$$g = V + 0.74(B - V) - 0.07. \quad (14)$$

For galaxies that do not have a known $B - V$, we have adopted the mean $B - V$ given by [Buta et al. \(1994\)](#) corresponding to the morphological type of the galaxy as listed by [Kennicutt et al. \(2003\)](#).

Table 3. XMP Objects

Object (1)	$D(\text{Mpc})$ (2)	$M(\text{H I}) (M_{\odot})$ (3)	m_g (4)	M_g (5)	$\log M(\text{H I})/L_g$ (6)	$[\text{O}/\text{H}]$ (7)	$\log M_{*}(M_{\odot})$ (8)	$\log \text{SFR}(M_{\odot} \text{ yr}^{-1})$ (9)
J0113+0052	15.80	3.39E+8	13.28 ^a	-17.69	-0.594	7.24	6.77	...
J0119-0935	24.80	1.38E+8	19.5	-12.47	1.10	7.31	6.06	-2.14
HS0122+0743	40.30	2.14E+9	15.7	-17.33	0.350	7.60	6.39	-1.17
J0126-0038	25.80	4.27E+8	18.4	-13.66	1.12	7.51	7.63	-2.93
UGCA20	8.63	2.00E+8	18.0	-11.68	1.58	7.60
UM133	22.40	4.37E+8	15.4	-16.35	0.052	7.63
J0204-1009	25.20	1.48E+9	17.1	-14.91	1.16	7.36	7.20	-1.54
J0205-0949	25.30	1.95E+9	15.3	-16.72	0.554	7.61
J0315-0024	90.90	2.51E+9	20.2	-14.59	1.52	7.41	7.77	...
UGC2684	5.95	8.71E+7	16.10 ^b	-12.77	0.784	7.60
SBS0335-052W	53.80	5.89E+8	19.0	-14.65	0.862	7.11
SBS0335-052E	54.00	4.17E+8	16.3	-17.36	-0.372	7.30 ^c	7.26 ^c	...
ESO489-G56	4.23	8.91E+6	15.6	-12.53	-0.110	7.49
HS0822+3542	11.72	8.71E+6	17.8	-12.54	-0.123	7.35	6.04	-1.99
HS0846+3522	36.30	3.09E+7	18.2	-14.60	-0.398	7.65
J0940+2935	7.23	2.51E+7	16.5	-12.80	0.231	7.65	6.30	-2.09
LeoA	1.54	2.34E+7	12.76 ^d	-13.18	0.049	7.30
KUG1013+381	19.90	1.41E+8	15.9	-15.59	-0.135	7.58	6.58	-1.46
UGCA211	15.50	1.70E+8	16.2	-14.75	0.282	7.56	7.18	-2.20
HS1033+4757	25.60	2.04E+8	17.5	-14.54	0.446	7.65	7.08	-1.89
HS1059+3934	48.10	7.59E+8	17.9	-15.51	0.628	7.62
J1105+6022	23.30	3.16E+8	16.4	-15.44	0.276	7.64	6.96	-1.53
SBS1129+576	26.40	6.46E+8	16.7	-15.41	0.598	7.36
J1201+0211	8.60	1.66E+7	17.6	-12.07	0.344	7.49	6.09	-1.99
SBS1121+540	17.20	4.37E+7	17.4	-13.78	0.080	7.64	6.02	-1.94
J1215+5223	3.33	1.23E+7	15.2	-12.41	0.078	7.43	6.01	-2.82
VCC0428	13.10	2.63E+7	17.0	-13.59	-0.064	7.64	6.20	-1.92
Tol65	37.90	7.24E+8	17.5	-15.39	0.656	7.54
J1230+1202	13.10	4.17E+7	16.7	-13.89	0.016	7.73	6.56	-1.69
UGCA292	3.41	3.89E+7	16.61 ^e	-11.05	1.12	7.28
GR8	1.43	4.37E+6	14.53 ^d	-11.25	0.092	7.65	6.02	-3.16
HS1442+4250	12.58	2.63E+8	15.9	-14.60	0.532	7.54	6.52	-2.08
HS1704+4332	33.60	6.46E+7	18.4	-14.23	0.070	7.55
J2053+0039	56.40	1.20E+9	19.4	-14.36	1.29	7.33	7.26	-1.73
J2104-0035	20.30	1.45E+8	17.9	-13.64	0.657	7.26 ^f	6.19	-2.01
J2150+0033	63.30	1.05E+9	19.3	-14.71	1.09	7.60	7.90	...
PHL293B	22.70	8.51E+7	17.2	-14.58	0.050	7.62	6.69	-1.52

Notes: The columns are as follows. (1): Source name. Some objects have other names: J0113+0052 = UGC772. (2): Distance. (3): H I gas mass. (4): Apparent g -band magnitude. Magnitudes are from [Filho et al. \(2013\)](#) unless the object is annotated with a superscript. In these cases, the g -mag is derived using a $B - V$ color transformation as described in the text, with the B and V magnitudes from the references listed below. (5): Absolute g -band magnitude. (6): Logarithm of the ratio of H I gas mass to g -band luminosity. (7):

Oxygen abundance $12 + \log \text{O}/\text{H}$. (8): Logarithm of the stellar mass. (9): Logarithm of the star formation rate. All data are from [Filho et al. \(2013\)](#) unless annotated with a superscript: *a*) [Patterson & Thuan \(1996\)](#); *b*) [van Zee et al. \(1996\)](#); *c*) [Izotov et al. \(2014\)](#); *d*) [de Vaucouleurs et al. \(1993\)](#); *e*) [Cook et al. \(2014\)](#); *f*) [Izotov et al. \(2012\)](#)

To compare the four samples with one another, we have attempted to minimize as much as possible systematic effects by using quantities that are derived in the same manner in the different samples. For example, the inclinations for the dwarf galaxies are derived using the same intrinsic ratio r_0 in both the GBT and XMP samples. The metallicities of many objects in the XMP sample came from publications from our group, ensuring that they are derived in the same way as the metallicities of the GBT sample. In any case, we expect small systematic differences in quantities such as stellar masses and metallicities to be overcome by the wide range of parameter space covered by these samples. Combining the GBT, XMP, Engelbracht and SINGS samples, we end up with a final sample of 151 objects. All data are

scaled, when necessary, to a distance based on $H_0 = 73.0 \text{ km s}^{-1} \text{ Mpc}^{-1}$.

Fig. 3 shows the metallicity histogram of the four samples. Examination of the figure shows that including the comparison samples extend the oxygen abundance range from 7.1 (1/40 solar) to 8.7 (solar), with the XMP and GBT low-mass low-luminosity galaxies covering the low-metallicity range, while the Engelbracht and SINGS higher-mass higher-luminosity galaxies span the high-metallicity range. Extending the metallicity range of the total sample extends the ranges of M_g (from -9 to -23 mag, Fig. 6), and of SFRs (Fig. 9) and sSFRs (Fig. 10).

Table 4. Engelbracht Objects

Object (1)	$D(\text{Mpc})^h$ (2)	$M(\text{H I}) (M_\odot)^h$ (3)	m_g (4)	M_g (5)	$\log M(\text{H I})/L_g$ (6)	$[\text{O}/\text{H}]$ (7)	$\log M_*(M_\odot)$ (8)	$\log \text{SFR}(M_\odot \text{ yr}^{-1})$ (9)
I Zw 18	13.9	1.25E+8	15.93 ^a	-14.79	0.133	7.17 ^f	6.42 ^f	-1.36 ^a
UGC 4483	5.00	6.15E+7	15.00 ^(a,d)	-13.49	0.345	7.46 ^f	5.16 ^f	-2.07 ^a
ESO 146-G14	21.3	1.44E+9	14.94 ^(b,e)	-16.70	0.430	7.66 ^h
DDO 187	2.07	1.05E+7	14.15 ^(b,b)	-12.43	0.001	7.79 ^h
Mrk 178	4.2	9.67E+6	14.03 ^a	-14.09	-0.699	7.88 ^h	...	-1.46 ^g
UM 462	13.2	2.11E+8	14.32 ^b	-16.28	-0.236	7.95 ^h	...	-0.248 ^h
UGC 4393	32.0	3.92E+9	13.12 ^b	-19.41	-0.219	7.95 ^h	...	-0.890 ^h
Mrk 1450	17.8	3.29E+7	15.63 ^a	-15.62	-0.779	7.84 ^f	7.55 ^f	-0.890 ^a
UM 448	76.9	6.18E+9	14.47 ^b	-19.96	-0.241	8.32 ^f	10.45 ^f	...
Mrk 170	18.4	3.88E+8	14.79 ^b	-16.53	-0.071	8.09 ^h
NGC 1569	1.45	2.45E+7	11.46 ^(b,b)	-14.35	-0.399	8.13 ^h	...	-1.52 ^h
Mrk 1094	37.4	2.07E+9	14.09 ^a	-18.77	-0.240	8.15 ^h	...	-0.90 ^a
NGC 3310	18.0	3.78E+9	10.82 ^b	-20.46	-0.655	8.18 ^h	...	0.693 ^h
NGC 1156	6.92	5.69E+8	11.89 ^(b,d)	-17.31	-0.217	8.19 ^h	...	-0.904 ^h
NGC 5253	2.79	6.11E+7	10.85 ^(b,d)	-16.38	-0.814	8.19 ^h	...	-0.833 ^h
NGC 4449	3.23	2.50E+8	9.97 ^(b,d)	-17.58	-0.682	8.23 ^h	...	-0.698 ^h
II Zw 40	10.4	3.61E+8	11.75 ^a	-18.34	-0.826	8.23 ^f	8.00 ^f	0.200 ^a
NGC 7714	39.1	5.49E+9	12.74 ^(b,d)	-20.22	-0.396	8.26 ^h	...	0.610 ^h
NGC 1510	10.0	1.60E+9	13.27 ^(b,b)	-16.73	0.464	8.33 ^h
NGC 4214	3.43	5.36E+8	10.02 ^(b,b)	-17.66	-0.383	8.36 ^h	...	-1.04 ^h
NGC 4670	21.0	1.15E+9	12.75 ^b	-18.86	-0.531	8.38 ^h	...	-0.037 ^h
NGC 1140	19.4	2.37E+9	12.77 ^(b,b)	-18.67	-0.141	8.38 ^f	8.72 ^f	...
NGC 2537	7.66	2.13E+8	11.94 ^b	-17.48	-0.712	8.44 ^h	...	-0.860 ^h
NGC 3628	7.9	3.24E+9	10.11 ^(b,b)	-19.38	-0.289	8.57 ^h	...	-0.950 ^h
NGC 2782	37.6	3.85E+9	11.75 ^b	-21.13	-0.915	8.59 ^h
NGC 5236	4.43	1.14E+10	8.04 ^(b,b)	-20.19	-0.067	8.62 ^h	...	0.146 ^h
NGC 3367	43.4	5.78E+9	11.91 ^b	-21.28	-0.798	8.62 ^h
NGC 4194	38.8	2.25E+9	12.93 ^b	-20.01	-0.700	8.67 ^h	...	0.571 ^h
NGC 2146	16.9	3.76E+9	11.13 ^(c,b)	-20.01	-0.477	8.68 ^h
NGC 2903	6.63	1.68E+9	9.37 ^(b,b)	-19.74	-0.719	8.68 ^h
Mrk 331	77.5	7.61E+9	14.61 ^b	-19.84	-0.103	8.76 ^h

Notes: The columns are as follows. (1): Source name. (2): Distance. (3): H I gas mass. (4): Apparent g -band magnitude derived using the $B - V$ color transformation as described in the text. Objects with two superscripts have both B and V magnitudes. Objects with one superscript have only B magnitudes. (5): Absolute g -band magnitude. (6): Logarithm of the ratio of H I gas mass to g -band luminosity. (7): Oxygen abundance $12 + \log \text{O}/\text{H}$. (8): Logarithm of the stellar mass. (9): Logarithm of the star formation rate. Superscripts refer to the following sources: *a*) Gil de Paz, Madore & Pevunova (2003); *b*) de Vaucouleurs et al. (1993); *c*) Héraudeau & Simien (1996); *d*) Taylor et al. (2005); *e*) Zackrisson et al. (2006); *f*) Izotov et al. (2014); *g*) Kennicutt et al. (2008); *h*) Engelbracht et al. (2008)

5 ANALYSIS

We now combine the four galaxy samples to explore possible correlations between various quantities.

5.1 H I mass-to-optical light ratio as a function of metallicity and absolute magnitude

We study here how the H I gas content depends on the galaxy's metallicity and luminosity. We first plot in Fig. 4 the $M(\text{H I})/L_g$ ratio against oxygen abundance for the galaxies in the four samples. The figure shows a clear trend of increasing ratios for lower metallicity galaxies. A linear least-square fit to the data, where $[\text{O}/\text{H}] = 12 + \log \text{O}/\text{H}$, gives:

$$\log[M(\text{H I})/L_g] = (-0.83 \pm 0.08) \times [\text{O}/\text{H}] + (6.47 \pm 0.66). \quad (15)$$

Staveley-Smith, Davies & Kinman (1992) found the $M(\text{H I})/L_g$ ratio to increase with decreasing galaxy luminosity. A linear least-square fit to our data gives (Fig. 5):

$$\log[M(\text{H I})/L_g] = (-0.30 \pm 0.03) \times \log L_g + (2.53 \pm 0.29). \quad (16)$$

The slope -0.30 of this relation is the same as the one obtained by Staveley-Smith et al. (1992), based on a smaller sample of 36 BCDs and low-surface-brightness dwarf galaxies, and spanning only 10 magnitudes in M_B (from -11 to -19 mag) instead of our luminosity range of 14 magnitudes in M_g (from -9 to -23 mag). Our slope is however steeper than the one of -0.2 obtained by Lee et al. (2002). The difference probably arises because of the more restricted luminosity range of the sample of Lee et al. (2002), spanning only 4 mag in M_B , from -14 to -18 mag.

5.2 Metallicity-luminosity and Mass-metallicity relations

Fig. 6 shows the well-known metallicity-luminosity relation for galaxies. Our fit (solid line)

$$[\text{O}/\text{H}] = (-0.12 \pm 0.01) \times M_g + (5.82 \pm 0.12) \quad (17)$$

Table 5. SINGS Objects

Object (1)	$D(\text{Mpc})^f$ (2)	$M(\text{H I}) (M_\odot)^f$ (3)	m_g (4)	M_g (5)	$\log M(\text{H I})/L_g$ (6)	$[\text{O}/\text{H}]^b$ (7)	$\log M_*(M_\odot)^c$ (8)	$\log \text{SFR}(M_\odot \text{ yr}^{-1})^e$ (9)
DDO 154	3.66	1.90E+8	13.46 ^(a,a)	-14.36	0.487	7.54	6.63	-2.63
DDO 53	2.42	2.76E+7	14.63 ^(a,a)	-12.29	0.477	7.60	6.35	-2.50
Holmberg I	4.74	1.92E+8	14.10 ^(a,d)	-14.28	0.523	7.61	6.80	-2.10
DDO 165	3.01	4.88E+7	13.23 ^(a,a)	-14.16	-0.024	7.63	6.83	-2.99
Holmberg II	4.89	1.24E+9	10.77 ^(a,a)	-17.68	-0.027	7.72	7.73	-0.940
NGC 5408	4.54	2.87E+8	11.60 ^(a,a)	-16.69	-0.266	7.81	8.29	-1.02
M81 Dw B	8.25	6.10E+7	15.01 ^a	-14.57	-0.091	7.84	6.36	-2.90
IC 2574	3.09	8.72E+8	10.62 ^(a,a)	-16.83	0.161	7.85	8.16	-1.31
NGC 2915	3.14	2.41E+8	12.79 ^(a,a)	-14.69	0.458	7.94	7.57	...
NGC 1705	5.94	1.28E+8	12.63 ^(a,a)	-16.24	-0.434	7.96	...	-0.990
NGC 1482	19.9	6.19E+8	12.81 ^(a,a)	-18.68	-0.728	8.11	9.99	...
NGC 4631	6.93	7.29E+9	9.43 ^a	-19.77	-0.093	8.12	9.76	0.040
Holmberg IX	2.97	2.56E+7	14.17 ^(a,a)	-13.19	0.084	8.14	...	-3.10
NGC 4536	28.9	6.86E+9	10.67 ^(a,a)	-21.63	-0.864	8.21	9.49	...
NGC 5713	29.5	1.05E+10	11.37 ^b	-20.98	-0.419	8.24	10.07	...
NGC 925	9.98	6.02E+9	10.58 ^b	-19.42	-0.036	8.25	9.48	-0.180
NGC 24	7.36	9.43E+8	12.05 ^b	-17.28	0.015	8.26	...	-1.22
NGC 3621	6.92	9.46E+9	9.20 ^b	-20.00	-0.072	8.27	9.43	0.070
NGC 4559	9.0	6.74E+9	10.44 ^b	-19.33	0.049	8.29	8.93	...
Mrk 33	24.2	5.95E+8	13.28 ^a	-18.64	-0.729	8.30
NGC 4736	4.40	6.00E+8	8.47 ^b	-19.75	-1.17	8.31	10.34	-0.700
NGC 5474	6.23	1.03E+9	11.31 ^b	-17.66	0.796	8.31	8.70	-1.07
NGC 2403	4.47	8.76E+9	8.60 ^b	-19.65	0.035	8.33	...	-0.400
NGC 2798	27.0	2.33E+9	12.73 ^b	-19.43	-0.453	8.34	10.04	...
NGC 3198	11.19	7.17E+9	10.04 ^b	-20.20	-0.272	8.34	9.85	...
NGC 3627	6.12	3.93E+8	9.04 ^b	-19.89	-1.41	8.34	10.57	-0.420
NGC 7331	15.0	9.31E+9	9.70 ^b	-21.18	-0.551	8.34	10.58	...
NGC 628	10.48	7.83E+9	9.80 ^a	-20.30	-0.274	8.35	9.57	...
NGC 4625	9.58	1.07E+9	12.90 ^b	-17.01	0.177	8.35	8.72	-1.28
NGC 4725	24.5	1.52E+10	10.48 ^b	-21.47	-0.454	8.35	10.58	...
NGC 7552	20.6	4.09E+9	11.09 ^b	-20.48	-0.628	8.35
NGC 2976	2.18	5.09E+7	10.76 ^(a,a)	-15.93	-0.713	8.36	8.97	-1.54
NGC 5033	15.7	1.30E+10	10.29 ^a	-20.69	-0.210	8.37
NGC 3521	7.7	3.43E+9	8.90 ^b	-20.53	-0.725	8.39	...	-0.130
NGC 5055	7.59	6.48E+9	9.12 ^b	-20.28	-0.348	8.40	10.76	-0.220
NGC 6946	5.52	3.64E+9	8.98 ^(a,a)	-19.73	-0.379	8.40	9.96	0.300
NGC 3031	1.68	7.79E+8	7.70 ^a	-18.43	-0.528	8.43
NGC 3773	10.1	5.99E+7	13.44 ^b	-16.58	-0.903	8.43	8.31	...
NGC 4254	36.3	2.38E+10	9.95 ^(a,a)	-22.85	-0.811	8.45	9.61	...
NGC 1097	15.4	7.98E+9	9.77 ^(a,a)	-21.17	-0.614	8.47	10.74	...
NGC 4321	13.1	2.00E+9	9.95 ^(a,a)	-20.64	-1.00	8.50	10.36	...
NGC 3034	5.68	5.33E+9	9.06 ^a	-19.71	-0.205	8.51
NGC 3184	9.27	2.13E+9	10.25 ^a	-19.59	-0.556	8.51	9.24	...
NGC 3049	21.9	1.31E+9	12.78 ^a	-18.92	-0.499	8.53	8.58	...
NGC 2841	11.52	4.68E+9	9.20 ^(b,a)	-21.11	-0.822	8.54	10.17	...
NGC 4826	3.54	1.23E+8	8.86 ^(a,a)	-18.89	-1.51	8.54	9.99	-1.10
NGC 5194	8.33	2.77E+9	8.86 ^a	-20.74	-0.902	8.55	...	0.220
NGC 1512	9.84	5.88E+9	10.95 ^(a,a)	-19.01	0.117	8.56	10.10	-0.570
NGC 3351	8.4	1.03E+9	10.23 ^b	-19.39	-0.791	8.60	10.28	-0.660

Notes: The columns are as follows. (1): Source name. (2): Distance. (3): H I gas mass. (4): Apparent g -band magnitude derived using the $B - V$ color transformation as described in the text. Objects with two superscripts have both B and V magnitudes. Objects with one superscript have only B magnitudes. (5): Absolute g -band magnitude. (6): Logarithm of the ratio of H I gas mass to g -band luminosity. (7): Oxygen abundance $12 + \log \text{O}/\text{H}$. (8): Logarithm of the stellar mass. (9): Logarithm of the star formation rate.

Superscripts refer to the following sources: *a*) [de Vaucouleurs et al. \(1993\)](#); *b*) [Moustakas et al. \(2010\)](#); *c*) [Skibba et al. \(2011\)](#); *d*) [Makarova \(1999\)](#); *e*) [Kennicutt et al. \(2008\)](#); *f*) [Kennicutt et al. \(2003\)](#)

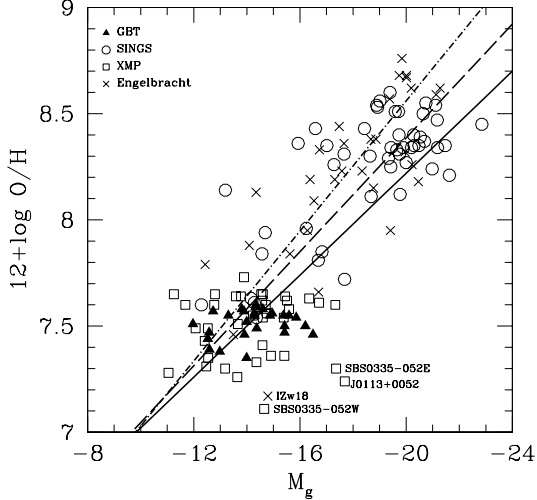


Figure 6. Plot of oxygen abundance versus absolute g magnitude for the GBT and the 3 comparison samples. The solid line represents the linear least-squares fit to all galaxies. For comparison, the metallicity-luminosity relations obtained by Skillman et al. (1989) (dash-dot line) and by Guseva et al. (2009) (dashed line) are also shown.

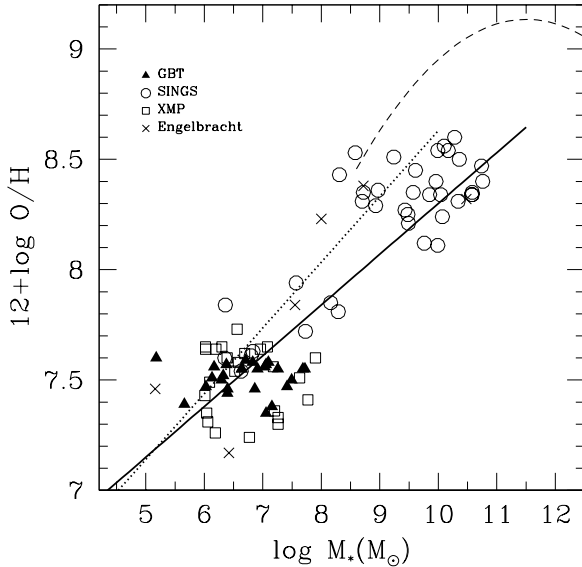


Figure 7. Plot of oxygen abundance versus stellar mass. The solid line represents the linear least-square fit to all galaxies in the GBT and the 3 comparison samples. The mass-metallicity relation derived by Tremonti et al. (2004) (dashed line) and by Lee et al. (2006) (dotted line) are also shown.

is in good agreement, within the errors, with the ones obtained for a local dwarf irregular galaxy sample by Skillman et al. (1989) (dot-dashed line), and for a local emission-line galaxy sample by Guseva et al. (2009) (dashed line). We note that four of the lowest-metallicity objects in our total sample, SBS 0335–052E, J0113+0052 = UGC 772, I Zw 18 and SBS 0335–052W (labeled in Fig. 6) deviate strongly from the above relation, being several magnitudes too bright for their oxygen abundance. These four galaxies are all undergoing strong bursts of star formation which increase significantly their luminosities. Izotov et al. (2011)

have shown that all galaxies undergoing strong starbursts also define their own luminosity-metallicity relation. This relation would have about the same slope, but would be shifted by several magnitudes towards higher luminosities. Similarly, Filho et al. (2013) found the metallicity-luminosity relation for their XMP galaxy sample to be shifted towards higher luminosities.

Fig. 7 shows the relation between stellar mass and metallicity. The best fit (solid line) is given by the equation:

$$[O/H] = (6.00 \pm 0.11) + (0.23 \pm 0.01) \times \log M_*. \quad (18)$$

where M_* represents the stellar mass in units of solar masses.

For comparison, we have also shown the relations derived by Tremonti et al. (2004) (dashed line) and Lee et al. (2006) (dotted line). It is seen that, in the region of stellar mass overlap ($8.6 \leq \log M_*/M_\odot \leq 11$), the Tremonti et al. (2004) curve is offset towards higher metallicities relative to ours by 0.2–0.7 dex. In this stellar mass range, our fit is mainly defined by the SINGS galaxies are determined by Moustakas et al. (2010), using both a theoretical (Kobulnicky & Kewley 2004) and an empirical (Pilyugin & Thuan 2005) strong-line abundance calibration. We have adopted here the abundances resulting from the empirical calibration. The shift of the Tremonti et al. (2004) curve is probably due to systematically too high oxygen abundances derived for their SDSS objects. Our fit is slightly flatter than the linear least-square fit $[O/H] = (5.65 \pm 0.23) + (0.30 \pm 0.03) \times \log M_*$ obtained by Lee et al. (2006). They are however consistent within 2σ .

5.3 The gas mass fraction as a function of metallicity

In Fig. 8 (left), we plot the distance-independent gas mass fraction (Eq. 11) as a function of the oxygen abundance. It is seen that while the high-metallicity ($[O/H] \geq 8.0$) SINGS galaxies span the range $0 \leq f_{gas} \leq 0.95$, the lower-metallicity GBT objects (with the exception of one galaxy, the BCD J1214+0940 with $f_{gas} = 0.27$) span the more restricted range $0.65 \leq f_{gas} \leq 0.99$, i.e. the vast majority of low-metallicity ($[O/H] \leq 7.8$) have more than 65% of their baryonic mass in gaseous form. This is consistent with the f_{gas} range 0.3–0.99 found by Bradford et al. (2015) for their sample of 148 isolated low-mass galaxies. As noted by those authors, the lower limit of ~ 0.3 for f_{gas} puts constraints on the internal feedback processes in low-mass and low-metallicity galaxies as they should not remove all of the galaxy’s atomic gas. We note also that in the low-metallicity regime, the GBT sample spans a larger range of gas mass fractions than the XMP sample of Filho et al. (2013): the vast majority of XMP galaxies have $f_{gas} \geq 0.85$. We have examined J1214+0940 to see if it possesses any particular characteristic that would make it relatively gas-poor, but found none. The median f_{gas} for the GBT sample is 0.94, while the mean f_{gas} is equal to 0.90 ± 0.15 . Our median value is higher than the value $f_{gas} = 0.82 \pm 0.13$ obtained by Bradford et al. (2015) for their larger SDSS dwarf galaxy sample. Evidently, the low-metallicity selection criterion selects out more gas-rich dwarf galaxies.

In Fig. 8 (right), we have plotted the atomic gas mass

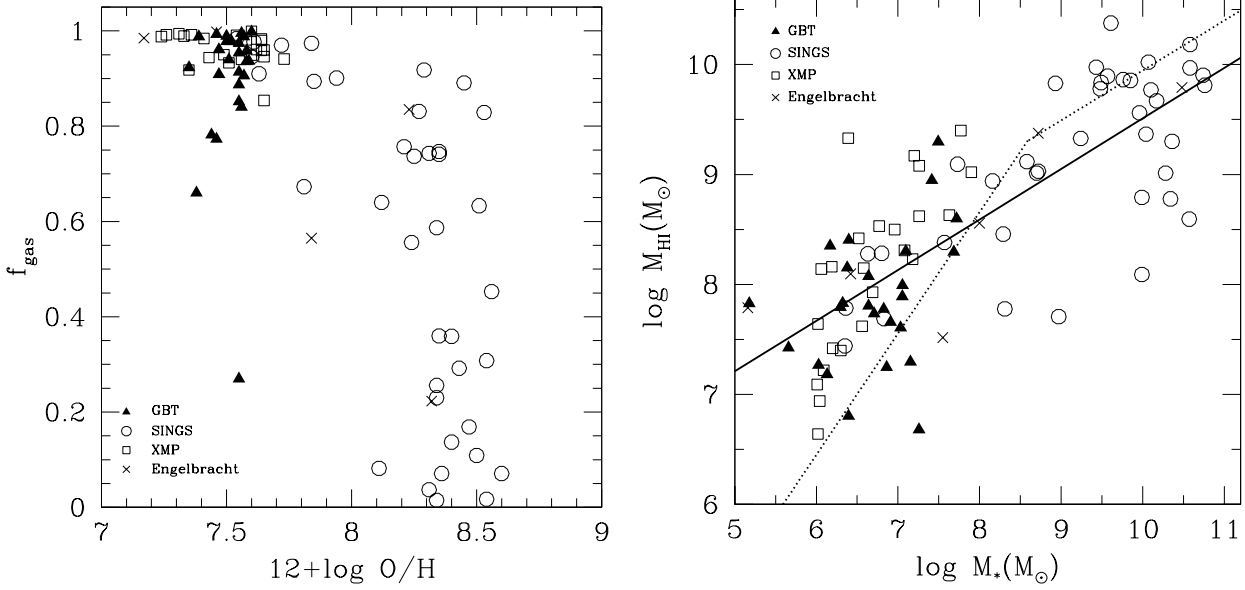


Figure 8. Plots of: (left) gas mass fraction versus metallicity; (right) neutral hydrogen mass versus stellar mass. The solid line shows the linear least-square fit to all galaxies in the GBT and the 3 comparison samples. It is described by the relation $\log M(\text{H I}) = (0.46 \pm 0.04) \times \log M_* + (4.91 \pm 0.31)$. The dashed line shows the fit obtained by [Bradford, Geha & Blanton \(2015\)](#) for their larger SDSS Data Release 8 galaxy sample.

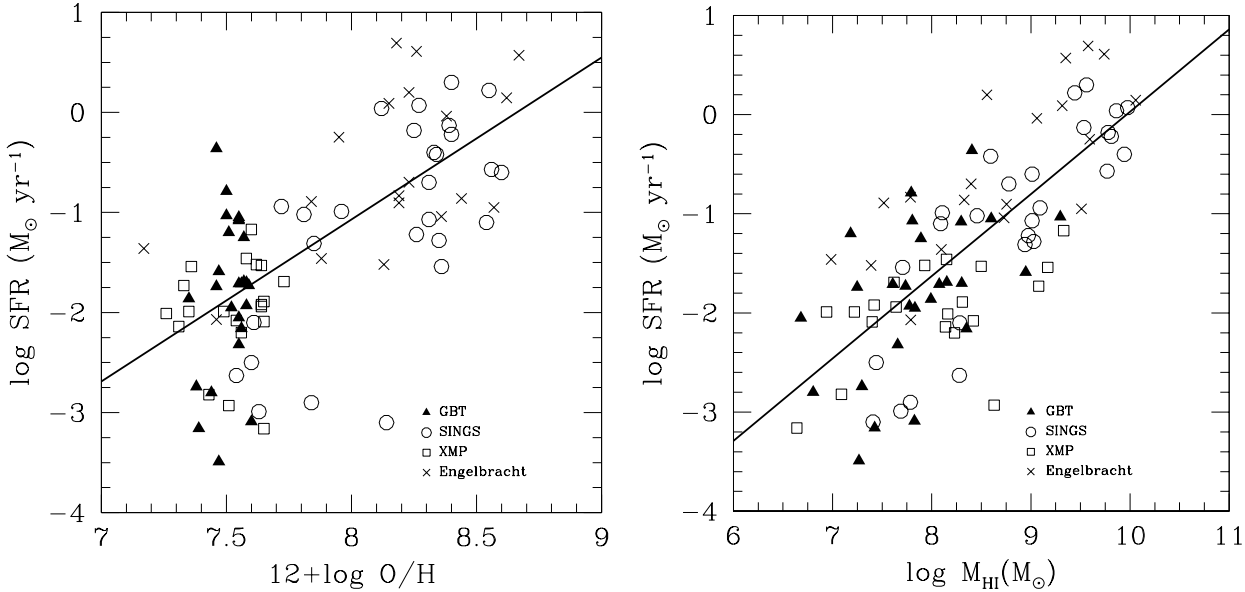


Figure 9. Plots of SFR versus: (left) metallicity. The solid line shows the least-square fit to all galaxies, described by the relation $\log \text{SFR} = (1.61 \pm 0.19) \times [\text{O}/\text{H}] - (14.03 \pm 1.50)$; (right) neutral hydrogen mass. The least-square fit is given by $\log \text{SFR} = (0.83 \pm 0.08) \times \log M(\text{H I}) - (8.27 \pm 0.67)$.

against the stellar mass. While our data for the GBT and the 3 comparison samples can be fitted by a single linear least-square fit (solid line), [Bradford et al. \(2015\)](#) obtained for their considerably larger sample of SDSS dwarf and non-dwarf galaxies a fit with a similar slope for non-dwarf galaxies ($M_* \geq 10^{8.6} M_\odot$) and a steeper slope for dwarf galaxies ($M_* \leq 10^{8.6} M_\odot$), with a break in the fit at about $10^{8.6} M_\odot$ (dashed line). We are not able to see the slope break in our data because of the smaller number of galaxies with $M_* \geq 10^{8.6} M_\odot$ in our sample.

5.4 Star formation rate

Fig. 9 (left) and Fig. 9 (right) show respectively the trends of SFR with oxygen abundance and H I mass. It is seen that there is a general correlation of increasing SFR for galaxies with higher metallicities (and hence higher stellar masses) and higher H I masses. However, when the SFR is normalized to the galaxy's stellar mass, i.e. if we plot the specific sSFR = SFR/M_* against metallicities (Fig. 10, left) and stellar masses (Fig. 10, right), then the trend is reversed. The galaxies with the lowest metallicities and stellar

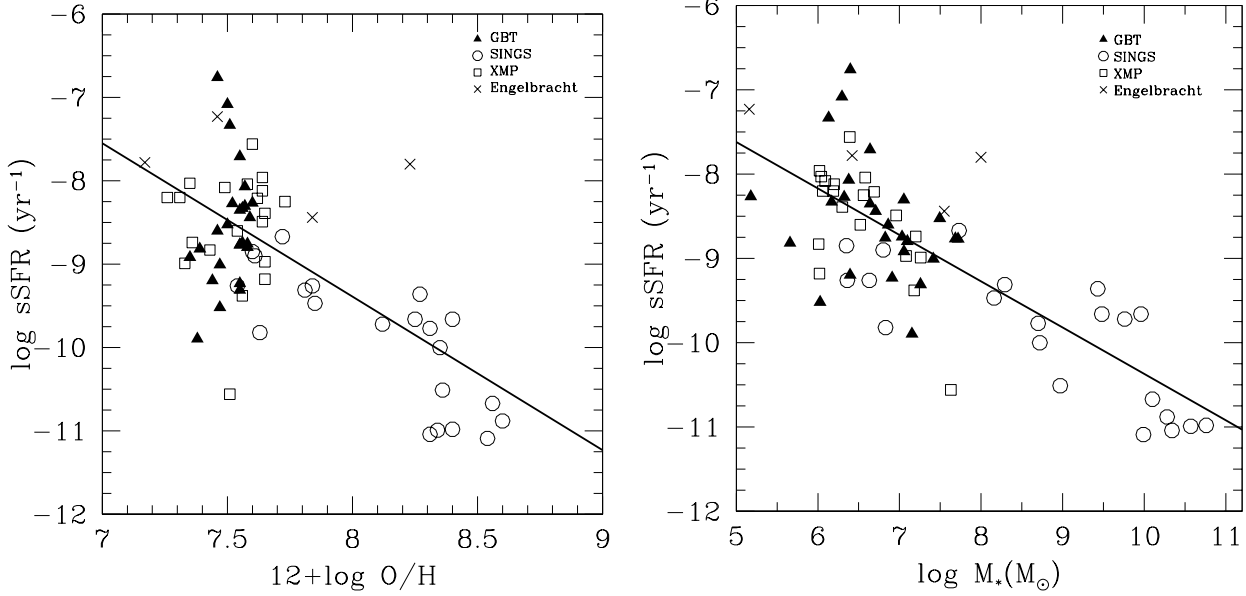


Figure 10. Plots of the specific star formation rate sSFR versus: (left) metallicity. The solid line shows the least-square fit to all galaxies, described by the relation $\log \text{sSFR} = (-1.85 \pm 0.25) \times [\text{O}/\text{H}] + (5.33 \pm 1.89)$; (right) stellar mass. The least-square fit is given by $\log \text{sSFR} = (-0.55 \pm 0.05) \times \log M_* - (4.87 \pm 0.40)$.

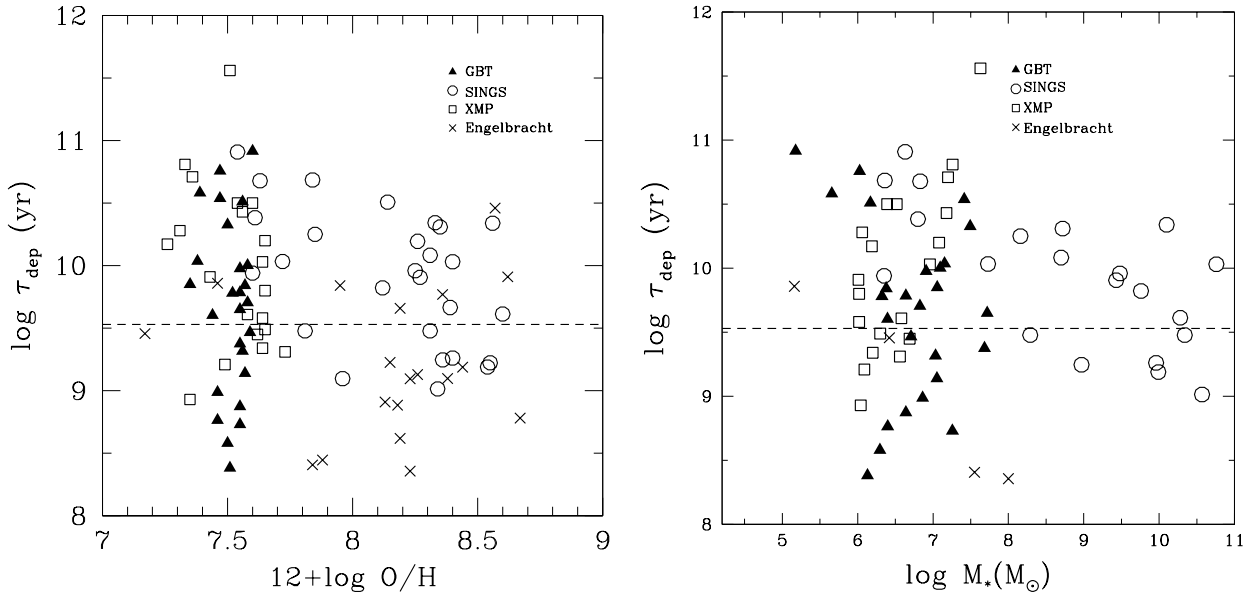


Figure 11. Plots of the gas depletion time versus (left) oxygen abundance, and (right) stellar mass, for all galaxies in the GBT and the 3 comparison samples. The dashed line in both plots shows the constant $\tau_{\text{dep}} = 3.4$ Gyr found by Schiminovich et al. (2010) for their *GALEX* Arecibo SDSS galaxy sample.

masses have the highest sSFRs. Similar trends were found by Filho et al. (2013) for their XMP galaxy sample and by Hunt et al. (2015) for a sample of metal-poor BCDs together with other galaxy samples from the literature.

5.5 Depletion time scales

We consider here the H I depletion time scale as defined by $\tau_{\text{dep}} \text{ (yr)} = M(\text{H I})/\text{SFR}$. This quantity measures the time left for a galaxy to form stars at the present rate before exhausting its gas supply. Galaxies with τ_{dep} less than the

Hubble time cannot make stars at the present rate without running out of fuel.

Fig. 11 (left) and Fig. 11 (right) show that there is no dependence of $\log \tau_{\text{dep}}$ on either oxygen abundance or M_* , with a large scatter. This is in agreement with the conclusion of Schiminovich et al. (2010) who find a relatively constant mean $\tau_{\text{dep}} = 3.4$ Gyr across their *GALEX* Arecibo SDSS galaxy sample. Hunt et al. (2015) also find a similar mean constant value, also with a large scatter (see also Filho et al. 2016). This mean value is shown by a dashed horizontal line in both panels of Fig. 11. While this line bisects well our

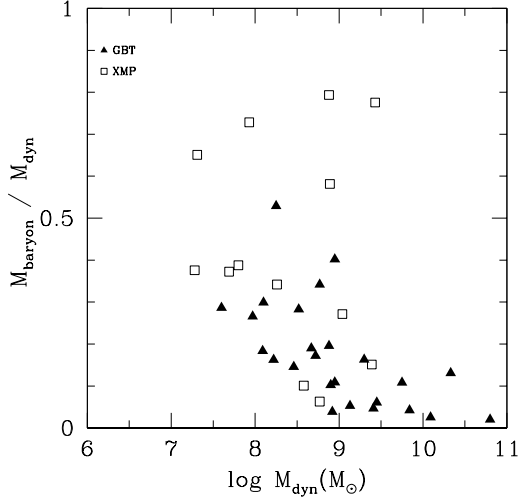


Figure 12. Plot of the baryon to dynamical mass fraction versus the dynamical mass for the GBT and XMP samples (the SINGS and Engelbract samples do not have published dynamical masses).

data, the scatter about the mean is ~ 1.5 dex on either side of the line. Using interferometric maps of a sample of spiral and dwarf irregular galaxies, Roychowdhury et al. (2015) have also found that the H I depletion time scale shows no strong dependence on metallicity within individual galaxies.

Why does $\text{sSFR} = \text{SFR}/M_*$ decrease steeply with increasing M_* (Fig. 10, right) while τ_{dep} or, equivalently, the inverse ratio which represents the H I-based star formation efficiency $\text{SFE} = \text{SFR}/M(\text{H I})$ remains relatively constant with M_* (Fig. 11, right)? Schiminovich et al. (2010) interpret this approximate constancy as indicating that external processes or feedback mechanisms controlling the gas supply are important for regulating star formation in massive galaxies. Our results show that these regulation mechanisms operate also in low-mass galaxies. Sánchez Almeida et al. (2014, 2015) have argued, based on observations of metallicity drops shown by localized starbursts in XMD galaxies, that accretion flows of external metal-poor gas may be a dominant regulation mechanism.

The majority of the GBT galaxies (77%) have τ_{dep} shorter than the Hubble time. This is consistent with the idea that their star formation histories are composed of short bursts lasting $\sim 10^{7-8}$ yr, interspersed with quiescent periods of $\sim 10^9$ yr (Thuan 2008). This appears also to be the case for the Engelbracht galaxies classified as BCDs. As for the XMP and SINGS galaxies, slightly more than half have τ_{dep} shorter than the Hubble time.

5.6 Baryonic mass fraction

Fig. 12 shows the plot of the baryonic mass fraction M_{baryon} versus the dynamical mass M_{dyn} for the GBT and XMP samples. The Engelbracht and SINGS samples do not have readily available dynamical mass data. No correlation is evident in the dynamical mass range between 10^7 and $10^{10.5} M_\odot$. The baryonic fraction of the GBT and XMP objects varies from 0.05 to 0.80, with a median value of ~ 0.2 . This is similar to the results of Bradford et al. (2015) who found for their large dwarf and non-dwarf SDSS galaxy sample a me-

dian baryon to dynamical mass ratio of 0.15 ± 0.18 , although this agreement may be somewhat fortuitous as these authors calculate M_{dyn} differently from us: they use the H I velocity width at 20% instead of 50% of maximum intensity, and the radius of the H I component is derived from a statistical relation between H I mass and H I radius. Our value is slightly smaller than the median baryon to dynamical mass ratio (within 3 optical scale lengths) of ~ 0.3 obtained by Lelli, Verheijen & Fraternali (2014), using H I rotation curves derived from interferometric maps. These baryonic mass fractions derived from H I rotation curves are likely more reliable. However, given that our dynamical masses are only approximate estimates from the H I velocity widths, the relatively good agreement implies that our dynamical mass estimates are not too far off.

5.7 Chemical Evolution

Knowledge of both the gas mass and the (ionized) gas metallicity allows us to test chemical evolution models of galaxies. In particular, for galaxies that evolve without gas infall or wind outflow, i.e. that can be described by closed box chemical evolution models, it is predicted that the effective stellar yield y_{eff} is a simple function of the metallicity Z_{gas} (in units of mass fraction) and the gas mass fraction f_{gas} .

$$y_{\text{eff}} = \frac{Z_{\text{gas}}}{\ln(1/f_{\text{gas}})}, \quad (19)$$

where $Z_{\text{gas}} = 12 \times (\text{O}/\text{H})$.

Here, we use the oxygen abundance as a proxy for the gas metallicity, and the factor 12 is the conversion from the number ratio O/H to oxygen mass fraction (Garnett 2002). If the galaxy truly evolves as a closed box, then the effective yield y_{eff} should be equal to the true yield y_{true} calculated from stellar evolution models. These models give $\log y_{\text{true}} \sim 2.4$ (Dalcanton 2007).

In Fig. 13 (left), we plot the histograms of y_{eff} for the four samples. The y_{true} value is shown by the solid vertical line. It is seen that while the y_{true} line bisects the data, there are many galaxies with y_{eff} inferior to or superior to y_{true} . Edmunds (1990) has shown that y_{eff} would be lower than y_{true} if metals have been lost from the galaxy through supernova-driven outflows, or if the current gas in the galaxy has been diluted with inflows of metal-poor gas. But how do we understand objects with effective yields greater than the theoretical yield? As discussed by Filho et al. (2013), this can be accounted for by either an underestimate of the true yield, or an overestimate of the effective yield, or both. For example, the true yield can be underestimated if the stellar Initial Mass Function (IMF) depends on metallicity, for example if the IMF slope flattens with decreasing metallicity (e.g. Bromm & Larson 2004). A top-heavy IMF would give a higher true yield. However, the spectral energy distributions of low-metallicity star-forming dwarf galaxies are well fitted with an IMF with a Salpeter slope, and do not show evidence for a top-heavy IMF (e.g. Izotov et al. 2011). It is more likely that the effective yields have been overestimated. In calculating it, we have assumed that the metallicity of the neutral gas is equal to that of the ionized gas, an assumption not likely to be true. In fact, we can estimate the ratio of the ionized gas metallicity to that of the neutral gas metallicity as it is roughly equal to the ratio of the effective yield to

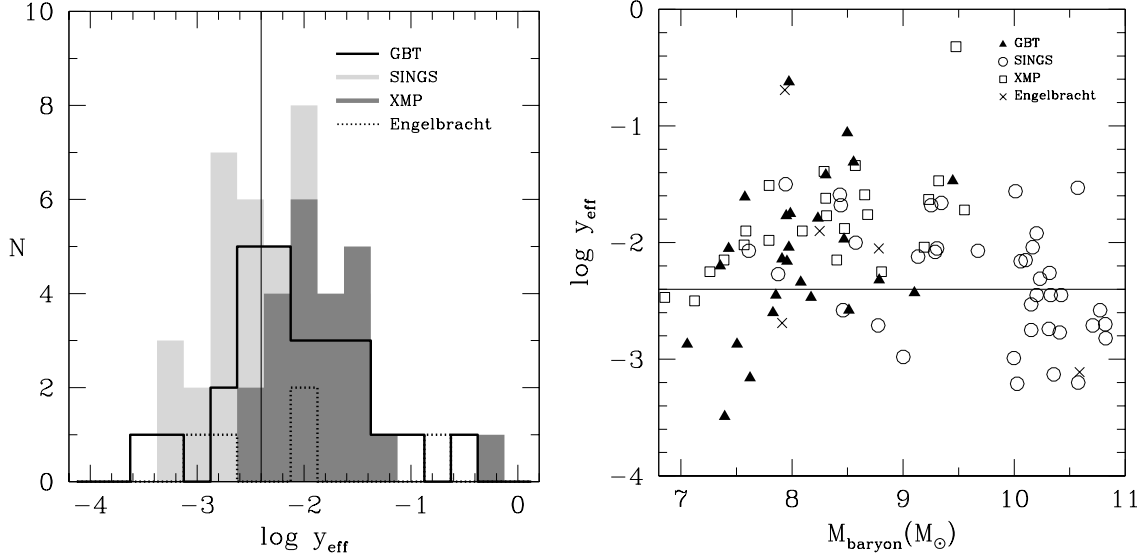


Figure 13. (left) Histogram of the effective yield y_{eff} for the 4 galaxy samples; (right) Plot of y_{eff} vs. M_{baryon} . The solid line shows the true yield for a closed-box model, $\log y = -2.4$ (Dalcanton 2007).

the true yield (Filho et al. 2013). Fig. 13 (right) shows that, for the majority of the GBT sample, this ratio ranges from about 1 to ~ 20 . This is very similar to the range of values found by Thuan, Lecavelier des Etangs & Izotov (2005) in their UV absorption line studies of BCDs. They show that the metallicity of their neutral gas is systematically smaller than that of their ionized gas, by a factor varying between ~ 20 for the higher-metallicity BCDs, and ~ 1.5 -2 for the lowest-metallicity BCDs, such as I Zw 18 or SBS 0335–052E. This metallicity difference is likely due to the fact that metals produced in the H II regions have not had time to diffuse out and mix with the H I gas in the outer regions. Thus the H I gas in the envelope of BCDs is relatively metal-free. This is in agreement with the results of Filho et al. (2013) who found the ratio of the metallicity of the ionized to that of the neutral gas to range between 1 and 10 for their XMP objects.

In summary, the distribution of the effective yields on either side of the true yield in Fig. 13 (left) can be understood as gas outflow and/or inflow of unenriched gas in the case of objects with $y_{\text{eff}} \leq y_{\text{true}}$, and a relatively metal-free H I envelope for objects with $y_{\text{eff}} \geq y_{\text{true}}$.

Fig. 13 (right) shows y_{eff} as a function of the baryonic mass of the galaxy. Both dwarf and non-dwarf galaxies display a large scatter on either side of the true yield line $\log y_{\text{true}} \sim -2.4$ (Dalcanton 2007). There is no evident variation of the effective yield with the baryonic mass of the galaxy. This result appears to be at odds with those obtained Garnett (2002) and Tremonti et al. (2004). Analyzing a sample of ~ 40 nearby spiral and irregular galaxies, Garnett (2002) found y_{eff} to be constant for galaxies with rotational velocities v_{rot} larger than $\sim 100 \text{ km s}^{-1}$, but to decrease by a factor of ~ 10 -20 below that threshold. Tremonti et al. (2004), using the spectroscopic data base of $\sim 53,000$ SDSS star-forming galaxies at $z \sim 0.1$, and using indirect estimates of the gas mass based on the H α luminosity, also found that y_{eff} decreases with decreasing baryonic galaxy mass. Both sets of authors attribute the decrease of the effective

yield at low galaxy masses to galactic winds removing metals more efficiently from the shallower potential wells of dwarf galaxies (see also Silich & Tenorio-Tagle 2001). However, Sánchez Almeida et al. (2014, 2015) have argued that the low metallicities of the XMD galaxies are an indicator of infall of pristine gas. This process would increase the effective yield of low-mass galaxies as compared to more massive galaxies. The real situation is likely described by both gas outflow and infall, so that the effective yields of the GBT dwarf galaxies do not decrease significantly as compared to the effective yields of more massive galaxies (like the SINGS galaxies).

6 SUMMARY AND CONCLUSIONS

New H I observations with the Green Bank Telescope (GBT) are presented for a sample of 29 extremely metal-deficient star-forming Blue Compact Dwarf (BCD) galaxies. The BCDs were selected from the spectral database of Data Release 7 of the Sloan Digital Sky Survey (SDSS) to have a well detected [OIII] $\lambda 4363$ line (for direct abundance determination) and an oxygen abundance $12 + \log \text{O}/\text{H} \leq 7.6$. Neutral hydrogen was detected in 28 galaxies, a 97% detection rate. For each galaxy, we have derived ancillary data from the SDSS optical spectrum such as oxygen abundance, star formation rate, and stellar mass.

Because of the narrow metallicity range of the GBT sample (the lower limit of $12 + \log \text{O}/\text{H}$ is 7.35), we have also added published H I and optical data for three complementary galaxy samples to extend the metallicity and mass range and study statistically how the H I content of a galaxy varies with various global galaxian properties. We have found the following:

- 1) The lowest-luminosity lowest-metallicity galaxies have the largest neutral hydrogen mass to light ratios, following the relation $M(\text{H I})/L_g \propto L_g^{-0.3}$, in good agreement with the dependence found in previous studies of galaxy

samples with a smaller luminosity range. Our derived mass-metallicity relation is also in good agreement with those derived by other authors.

2) Metal-deficient low-mass dwarf galaxies are gas-rich. The median gas mass fraction of the GBT sample is 0.94, while its mean gas mass fraction is 0.90 ± 0.15 . The vast majority of the GBT galaxies have more than 65% of their baryonic mass in gaseous form. The existence of a lower limit, also found for larger dwarf samples, puts stringent constraints on feedback mechanisms in low-mass galaxies as they should not remove all of the galaxy's atomic gas.

3) The H I depletion time is independent of metallicity or stellar mass. Although there is a large scatter about the median value of 3.4 Gyr, the relative constancy of the gas depletion time implies that external processes or feedback mechanisms that control the gas supply are important for regulating star formation in both low- and high-mass galaxies.

4) The ratio of the baryonic mass to the dynamical mass varies over a wide range, from 0.05 to 0.80, with a median value of ~ 0.2 and no dependence on the dynamical mass.

5) About 35% of the GBT galaxies have an effective yield less than the true yield, which can be understood as the result of the loss of metals due to supernova-driven outflows, and/or the consequence of dilution by inflows of metal-poor gas. However, the remaining 65% show an effective yield larger than the true yield. This can be understood if the metallicity of the neutral gas is lower than the metallicity of the ionized gas by a factor ~ 1.5 –20, as UV absorption studies of BCDs also show.

7 ACKNOWLEDGEMENTS

T.X.T. thanks the support of NASA grant GO4-15084X. The SDSS is managed by the Astrophysical Research Consortium for the Participating Institutions. This research made use of the NASA/IPAC Extragalactic Database (NED) which is operated by the Jet Propulsion Laboratory, California Institute of Technology, under contract with NASA.

REFERENCES

- Abazajian K. et al., 2005, *AJ*, 129, 1755
 Abazajian K. et al., 2009, *ApJS*, 182, 543
 Adelberger K. L., Steidel C. C., Pettini M., Shapley A. E., Reddy N. A., Erb D. K., 2005, *ApJ*, 619, 697
 Ahn C. P. et al., 2013, *ApJS*, 211, 17A
 Bessel M. S., 2005, *Ann. Rev. Astron. Astrophys.*, 43, 293
 Bradford J. D., Geha M. C., Blanton M. R., 2015, *ApJ*, 809, 146
 Brinchmann J., Charlot S., White S. D. M., Kauffmann G., Heckman T., 2004, *MNRAS*, 351, 1151
 Bromm V., Larson R. B., 2004, *Ann. Rev. Astron. Astrophys.*, 42, 79
 Buta R., Mitra S., de Vaucouleurs G., Corwin Jr. H.G., 1994, *AJ*, 107, 1
 Cook D. O. et al., 2014, *MNRAS*, 445, 881
 Dalcanton J. J., 2007, *ApJ*, 658, 941
 de Vaucouleurs G., de Vaucouleurs A., Corwin H. G., Buta R. J., Paturel G., Fouque P., 1991, *Third Reference Catalogue of Bright Galaxies (RC3)*, Springer-Verlag: New York
 Edmunds M. G., 1990, *MNRAS*, 246, 678
 Ekta B., Pustilnik S. A., Chengalur J. N., 2009, *MNRAS*, 397, 963
 Ekta B., Chengalur J. N., 2010, *MNRAS*, 403, 295
 Engelbracht C. W., Rieke G. H., Gordon K. D., Smith J.-D. T., Werner M. W., Moustakas J., Willmer C. N. ., Vanzi L., 2008, *ApJ*, 678, 804
 Filho M. E. et al., 2013, *A&A*, 558, A18
 Filho, M. E., Sánchez Almeida J., Amorín R.; Muñoz-Tuñón C., Elmegreen B. G., & Elmegreen D. M., 2016, *ApJ*, 820, 109
 Garnett D. R., 2002, *ApJ*, 581, 1019
 Geha M., Blanton M. R., Masjedi M., West A. A., 2006, *ApJ*, 653, 240
 Gil de Paz A., Madore B. F., Pevunova O., 2003, *ApJS*, 147, 29
 Giovanelli R., Haynes M. P., Salzer J. J., Wegner G., da Costa L. N., Freudling W., 1994, *AJ*, 108, 33S
 Guseva N. G., Papaderos P., Meyer H. T., Izotov Y. I., Fricke K. J., 2009, *A&A*, 503, 61
 Héraudeau Ph., Simien F., 1996, *A&AS*, 118, 111
 Hogg D. E., Roberts M. S., Haynes M. P., Maddalena R. J., 2007, *AJ*, 134, 1046
 Huchtmeier W. K., Krishna G., Petrosian A., 2005, *A&A*, 434, 887
 Hunt L. et al., 2012, *MNRAS*, 427, 906
 Hunt L. et al., 2015, *A&A*, 583, 114
 Izotov Y. I., Thuan T. X., 1999, *ApJ*, 511, 639
 Izotov Y. I., Thuan T. X., Guseva N. G., 2005, *ApJ*, 632, 210
 Izotov Y. I., Guseva N. G., Thuan T. X., 2011, *ApJ*, 728, 161
 Izotov Y. I., Thuan T. X., Guseva N. G., 2012, *A&A*, 546, A122
 Izotov Y. I., Guseva N. G., Fricke K. J., Krügel E., Henkel C., 2014, *A&A*, 570, A97
 Izotov Y. I., Orlitova I., Schaerer D., Thuan T. X., Verhamme A., Guseva N. G., Worseck G., 2016, *Nature*, 529, 178
 Jester S. et al., 2005, *AJ*, 130, 873
 Kauffmann G. et al., 2003, *MNRAS*, 341, 33
 Kennicutt R. C., 1998, *ApJ*, 498, 541
 Kennicutt R. C. et al., 2003, *PASP*, 115, 928
 Kennicutt R. C., Lee J. C., Funes J. G., Sakai S., Akiyama S., 2008, *ApJS*, 178, 247
 Kent B. R. et al., 2008, *AJ*, 136, 713
 Kobulnicky H. A., Kewley L. J., 2004, *ApJ*, 617, 240
 Koribalski B. S., et al., 2004, *AJ*, 128, 16
 Lee H., Skillman E. D., Cannon J. M., Jackson D. C., Gehrz R. D., Polonski E. F., Woodward C. E., 2006, *ApJ*, 647, 970
 Lee J. C., Salzer J. J., Impey C., Thuan T. X., Gronwall C., 2002, *ApJ*, 124, 3088
 Lelli F., Verheijen M., Fraternali F., 2014, *A&A*, 566, A71
 Lequeux J., 1983, *A&A*, 125, 394
 Loose H.-H., Thuan T. X., 1985, in *Star-forming dwarf galaxies and related objects*, ed. D. Kunth, T. X. Thuan & J. T. T. Van (Gif-sur-Yvette: Editions Frontieres), 73

- Mamon G. A., Tweed D., Thuan T. X., Cattaneo A., 2012, in *Dwarf galaxies: keys to galaxy formation and evolution*, eds. P. Papaderos, S. Recchi & G. Hensler (Berlin, Heidelberg: Springer-Verlag).
- Makarova L., 1999, *A&AS*, 139, 491
- Morales-Luis A. B., Sánchez Almeida J., Aguerri J. A. L., Muñoz-Tuñón C., 2011, *ApJ*, 743, 77
- Mould J. R., et al., 2000, *ApJ*, 529, 786
- Moustakas J., Kennicutt R. C., Tremonti C. A., Dale D. A., Smith J.-D. T., Calzetti D., 2010, *ApJS*, 190, 233
- Murphy E. J., Helou G., Kenney J. D. P., Armus L., Braun R., 2008, *ApJ*, 678, 828
- Noeske K. G., Guseva N. G., Fricke K. J., Izotov Y. I., Papaderos P., Thuan T. X., 2000, *A&A*, 361, 33
- Patterson R. J., Thuan T. X. 1996, *ApJS*, 107, 103
- Paturel G., Petit C., Prugniel P., Theureau G., Rousseau J., Brouty M., Dubois P., Cambrésy L., 2003, *A&A*, 412, 45
- Pilyugin L. S., Ferrini F., 2000, *A&A*, 354, 874
- Pilyugin L. S., Thuan T. X., 2005, *ApJ*, 631, 231
- Popping A., Braun R., 2011, *A&A*, 528A, 28
- Pustilnik S. A., Martin J.-M., 2007, *A&A*, 464, 859
- Riess A. G. et al., 2011, *ApJ*, 730, 119
- Roychowdhury S., Huang M.-L., Kauffmann G., Wang J., Chengalur J. N., 2015, *MNRAS*, 449, 3700
- Sánchez Almeida J., Morales-Luis A. B., Muñoz-Tuñón C.; Elmegreen D. M., Elmegreen B. G., Méndez-Abreu J., 2014, *ApJ*, 783, 45
- Sánchez Almeida J. et al., 2015, *ApJ*, 810, L15
- Sánchez Almeida J., Pérez-Montero E., Morales-Luis A. B., Muñoz-Tuñón C., García-Benito R., Nuza S. E., Kitaura F. S., 2016, *ApJ*, 819, 110
- Sánchez-Janssen R., Méndez-Abreu J., Aguerri J. A. L., 2010, *MNRAS*, 406, L65
- Sargent W. L., Searle L., 1970, *ApJ*, 162, L155
- Schimminovich D. et al., 2010, *MNRAS*, 408, 919
- Silich S., Tenorio-Tagle G., 2001, *ApJ*, 552, 91
- Skibba R. A. et al., 2011, *ApJ*, 738, 89
- Skillman E. D., Kennicutt R. C., Hodge P. W., 1989, *ApJ*, 347, 882
- Springob C. M., Haynes M. P., Giovanelli R., Kent B. R., 2005, *ApJS*, 160, 149
- Staveley-Smith L., Davies R. D., Kinman T. D., 1992, *MNRAS*, 258, 334
- Steffen M., Prakatavicius D., Caffau E., Ludwig H.-G., Bonifacio P., Cayrel R., Kucinskas A., Livingston W. C., 2015, *A&A*, 583, A57
- Steidel C. C., Adelberger K. L., Shapley A. E., Pettini M., Dickinson M., Giavalisco M., 2003, *ApJ*, 592, 728
- Stierwalt S., Haynes M. P., Giovanelli R., Kent B. R., Martin A. M., Saintonge A., Karachentsev I. D., Karachentseva V. E., 2009, *AJ*, 138, 338
- Taylor V. A., Jansen R. A., Windhorst R. A., Odewahn S. C., Hibbard J. E., 2005, *ApJ*, 630, 784
- Thuan T. X., 2008, in *Low-metallicity star formation: from the first stars to dwarf galaxies*, ed. L. Hunt, S. C. Madden, & R. Schneider (Cambridge: Cambridge Univ. Press), 348
- Thuan T. X., Martin G., 1981, *ApJ*, 247, 823
- Thuan T. X., Izotov Y. I., 2005, *ApJ*, 627, 739
- Thuan T. X., Lecavelier des Etangs, A., Izotov Y. I., 2005, *ApJ*, 621, 269
- Thuan T. X., Izotov Y. I., Foltz C. B., 1999, *ApJ*, 525, 105
- Thuan T. X., Lipovetsky V. A., Martin J.-M., Pustilnik S. A., 1999, *A&AS*, 139, 1
- Tremonti C. A. et al., 2004, *ApJ*, 613, 898
- van Zee L., Haynes M. P., Salzer J. J., 1997, *AJ*, 114, 2479
- York D. G. et al., 2000, *AJ*, 120, 1579
- Zackrisson E., Bergvall N., Marquart T., Östlin G., 2006, *A&A*, 452, 857